Dynamic nucleotide flipping drives super-resolution fluorescence activation in the RhoBAST RNA aptamer

Xiaoqing Tai[1,6], Mengqi He[1,6], Christoph Mitteregger[2,6], Huiqin You[1], Peng Xiong[3,4], Zejia Hu[1], Xinyue Bao[1], Xin Shen[1], Hongcheng Li[1], Yu Li[5], Jinzhu Zhang[1,*], Ronald Micura[2,*] and Aiming Ren[1,*]

[1]Department of Cardiology of The Second Affiliated Hospital and Life Sciences Institute and School of Medicine and Liangzhu Laboratory, Zhejiang University, Hangzhou 310058, China

[2]Institute of Organic Chemistry, Center for Molecular Biosciences Innsbruck, Leopold Franzens University, Innsbruck A6020, Austria

[3]School of Biomedical Engineering, Division of Life Sciences and Medicine, University of Science and Technology of China, Hefei, Anhui 230026, China

[4]Suzhou Institute for Advanced Research, University of Science and Technology of China, Suzhou, Jiangsu 215123, China

[5]Department of Computer Science and Engineering, The Chinese University of Hong Kong, Hong Kong SAR 000000, China

[6]These authors contributed equally to this work.

*Email: aimingren@zju.edu.cn (AR), ronald.micura@uibk.ac.at (RM) and jinzhuzhang@zju.edu.cn (JZ).

Abstract

Super-resolution imaging with RhoBAST fluorogenic RNA aptamer sheds new light on decoding RNA dynamics with high spatiotemporal resolution. To uncover the molecular basis underlying its exceptional photophysical properites, we determined the first free-form structure of RhoBAST, along with its ligand-bound complexes with TMR-DN and related analogs. RhoBAST adopts an inverted 'V'-shaped architecture, with the fluorophore accommodated between the J2/3 and L3 loops. Comparative structural analyses reveal that nucleotide G38 undergoes a pronounced conformational transition—from an inward-facing to an outward-flipped orientation—upon ligand binding. Structure-guided mutagenesis and complementary biophysical assays, including fluorescence spectroscopy, surface plasmon resonance, and 2-aminopurine kinetics, establish that this dynamic nucleotide flipping facilitates rapid ligand turnover and fluorescence flickering, the hallmark of super-resolution imaging. These findings uncover a previously unrecognized nucleotide-flipping mechanism in a fluorogenic RNA aptamer, providing a structural and mechanistic blueprint for the rational design of next-generation super-resolution RNA imaging tools.

Introduction

Super-resolution imaging has revolutionized the field of molecular and cellular biology by surpassing the classical diffraction limit of light microscopy, enabling visualization of cellular structures or biomolecules at nanometer-scale resolution. This advancement has been particularly transformative for uncovering the spatial organization and dynamic interactions of biomolecules within their native cellular environments. As the carrier of genetic information and the versatile regulator, RNA plays a central role in the complex dynamic cellular processes, including transcription, splicing, localization, translation, and degradation, which are essential for maintaining cellular homeostasis and overall organismal health. Tracking individual RNA molecules with sufficient clarity at single-molecule resolution within cells, not only pushes the boundaries of what can be visualized within cells but also drives deeper mechanistic understanding of fundamental biological functions of RNA molecules[1,2].

Since the introduction of live-cell RNA imaging in 1997[3,4], significant progress has been made employing fluorescent proteins-based systems to track the dynamics of RNA, including MS2/MCP[5], PP7/PCP[6], boxB/λN22[7], and CRISPR-dCas[8]. These traditional live-cell RNA imaging methods have greatly advanced our understanding of the spatiotemporal dynamics and biological roles of RNA molecules[3,4]. Despite their utility, these techniques face challenges, such as high background fluorescence from unbound fluorescent proteins and potential disruptions to RNA structure and function due to tagging sequence insertion, which limit their widespread application. To overcome these limitations, fluorescent light-up aptamers (FLAPs) were developed through systematic evolution of ligands by exponential enrichment (SELEX). FLAPs are a unique class of RNA sequences that specifically bind to small-molecule dyes and activate their fluorescence. When fused to RNA sequences of interest, these aptamers enable live-cell RNA imaging with high signal-to-noise ratios and low background fluorescence. Their small size, ease of use, and superior photophysical properties make FLAPs promising tools for live-cell RNA imaging with fluorescent dyes[9]. Several FLAPs and their corresponding fluorophore ligands have been developed and

extensively characterized, including Spinach-DFHBI[10], Broccoli-BI[11], Mango II-TO1-Biotin[12], Corn-DFHO[13], Pepper-HBC[14], and Clivia-NBSI[15]. These aptamers span nearly the entire visible spectrum, enabling multicolor RNA imaging. However, they still face challenges in combining high affinity with optimal photophysical attributes, such as fluorescent brightness, resistance to photobleaching[9,16] and suitability for super-resolution imaging.

A fluorophore-quencher conjugate dye consists of a fluorescent molecule (fluorophore) paired with a quencher that suppresses fluorescence until a specific interaction occurs, such as the binding of a complementary nucleic acid or an aptamer. These conjugates are widely used in molecular imaging, biosensing, and live-cell studies due to their high signal-to-noise ratio and precision. Recently, RhoBAST (Rhodamine Binding Aptamer for Super-resolution Imaging Techniques), identified through SELEX screening and strategic mutations of an RNA library derived from the sulfonamide B-binding aptamer SRB-2, was reported to bind the tetramethylrhodamine (TMR) in the fluorophore-quencher conjugate TMR-dinitroaniline (TMR-DN) with high affinity (K_d = 15 ± 1 nM), exhibiting significantly enhanced brightness and stability[17]. The presence of the quenching group (DN) in TMR-DN reduces background fluorescence in the absence of aptamers, ensuring high specificity. Owing to the rapid dissociation and association kinetics, the fluorescence of the RhoBAST/TMR-DN system exhibits a blinking behavior, which represents an advanced fluorescence feature that is currently absent in other fluorescent RNA aptamers. Benefiting from this fluorescence blinking property, the RhoBAST/TMR-DN system became the first photobleaching-resistant FLAP optimized for live-cell single-molecule localization microscopy (SMLM), enabling high-resolution imaging without photobleaching interference.

Recently, Zhou et al. optimized the RhoBAST/TMR-DN system and achieved super-resolution imaging of the demethylation process of endogenous proteins[18]. This study extends the application of high-resolution imaging by RhoBAST from visualizing subnuclear RNA localization to visualizing the demethylation process of endogenous

proteins, while indicating the enormous application potential of RhoBAST/TMR-DN. Additionally, biRhoBAST-TMR2, generated by dimerization of RhoBAST and its fluorophore TMR, enables high-contrast tracing of single mRNA molecules[19]. SpyRho, a novel dye developed by attaching the carboxyl group to the 3-position of the TMR's benzene moiety to form a spiral ring structure, exhibits high membrane permeability[20]. SpyRho achieves high brightness and fluorogenicity by shifting the equilibrium between its non-fluorescent spirocyclic form and a fluorescent quinoid form. SpyRho's exceptional performance in SMLM and its role in generating the first super-resolved stimulated emission depletion (STED) images of specifically labeled RNA in live mammalian cells represent a significant advancement over other FLAPs.

To elucidate how this bright, flicker-fluorescent aptamer recognizes fluorophores and enhances their fluorescence with superior photophysical properties, we employed X-ray crystallography to determine the first tertiary structure of RhoBAST in its free-form, as well as the bound-form structures in complex with TMR-DN, TMR and 5-TAMRA, respectively. Comparison of the three-dimensional structures of free-form and ligand-bound RhoBAST, combined with site-directed mutagenesis analysis, revealed a previously unrecognized base-flipping mechanism underlying the super-resolution fluorescence activation process of FLAP, which was further validated by surface plasmon resonance (SPR) and 2-aminopurine (2-AP) fluorescence assays. Collectively, our study reveals, for the first time, a nucleotide-flipping mechanism that establishes the structural and mechanistic foundation of super-resolution FLAPs. By elucidating the molecular basis of fluorescence activation, these findings pave the way for the rational design of next-generation FLAPs with improved brightness, stability, and photophysical performance, broadening their applications in live-cell RNA imaging, tracking, and dynamic studies of RNA biology.

Results

Crystallization and tertiary fold of free-form and TMR-DN-bound RhoBAST

The chemical structure of the fluorophore tetramethylrhodamine (TMR) conjugated with the quenching group dinitroaniline (DN) is shown in Fig. 1a, while the initial RNA sequence selected through SELEX is presented in Extended Data Fig. 1a. To obtain high-quality crystals of RhoBAST, we varied the length of the stem P2 and the sequence of its terminal loop L2. Numerous *in vitro* transcribed RhoBAST constructs were screened for crystallization both in the absence and presence of TMR-DN. Ultimately, high-quality crystals of both free-form and TMR-DN-bound form were obtained using a 57-nucleotide (nt) construct of wild-type RhoBAST (RhoBAST-WT), as shown in Fig. 1b. To validate the fluorescence activation capability of RhoBAST-WT used in crystallization, we measured the three-dimensional fluorescence spectra of TMR-DN in the presence and absence of RhoBAST-WT. Free TMR-DN in aptamer SELEX buffer with Tween 20 (ASBT) solution exhibited a maximum excitation wavelength of 555 nm and a maximum emission wavelength of 580 nm, with minimal fluorescence intensity (Fig. 1c, Extended Data Fig. 1b). Upon binding to RhoBAST-WT, the spectra showed a redshift, with excitation and emission wavelengths shifting to 565 nm and 585 nm, respectively, along with a significant fluorescence intensity increase (Fig. 1c, Extended Data Fig. 1b).

The tertiary structures of the free-from (Fig. 1d-e) and TMR-DN-bound (Fig. 1f-g) RhoBAST were determined at resolutions of 2.53 Å and 2.8 Å, respectively. Detailed X-ray crystallographic statistics are provided in Supplementary Table 1. Both free-form (Fig. 1d-e) and TMR-DN-bound-form (Fig. 1f-g) RhoBAST structures adopt an inverted 'V'-shaped scaffold, comprising three stems: P1 (orange), P2 (purple), and P3 (green), and a central junction, J2/3 (cyan). Alignment of the free-form and TMR-DN-bound-form RhoBAST structures reveals a consistent overall fold, with minor conformational variation in TMR-DN binding pocket (Extended Data Fig. 2a). Stems P1 and P3 stack continuously and form an elongated, stable helix, while stem P2 along with junction

region J2/3 form a continuous stacking interaction (Fig. 1d-g, Extended Data Fig. 2b-c). The junction J2/3 comprises seven nucleotides (from U22 to A28; Fig. 1b, 2b), with U22 and A28 forming a canonical Watson-Crick (WC) base pair that stacks directly on the top of stem P2 (Fig. 1h). Within this arrangement, nucleotides A28-G29 and U7-C8 adopt splayed conformations in the tertiary structure, bridging P2 with J2/3 and P1 with P3 through continuous coaxial stacking interactions (Fig. 1d-g, i). These stacking interactions are further stabilized by two hydrogen bonds: one between the O2' of U7 (P1) and the phosphate oxygen of G29 (P3), and another between the O2' atom of A28 (J2/3) and the phosphate oxygen of C8 (P2) (Fig. 1i). The terminal loop L3 of stem P3 and junction J2/3 form extensive long-distance interactions in the upper region of the structure (Fig. 1d-g). It was noted that the bound TMR-DN is located at the intersection of L3 and J2/3 in the complex structure (Fig. 1f-g).

Long-range interaction involved in the stabilization of RhoBAST

As mentioned before, extensive long-range interactions were identified predominantly between J2/3 and L3 in the upper part of both the free-from and TMR-DN-bound structures (Fig. 2a-b).These interactions can be organized into three spatially distinct layers: the upper and middle layers, each defined by a base triplet (A24-A42-A37 and G26-A43-A36, respectively), and the bottom layer, comprising two canonical Watson–Crick base pairs (G23-C44 and G27-C35) (Fig. 2c and Extended Data Fig. 3a). Specifically, at the upper layer, the A24 (J2/3)-A42 (L3)-A37 (L3) base triplet is stabilized by multiple interactions: A24 (J2/3) hydrogen-bonds with O2' of U41 (L3) and engages in a non-canonical pair with A42 (L3), while A42 (L3) forms three additional hydrogen bonds with the sugar moiety of A37 (L3) (Fig. 2d and Extended Data Fig. 3d). In the middle layer, the base of G26 (J2/3) forms two hydrogen bonds with the phosphate oxygen of A42 (L3), as well as one non-canonical base pair with the base of A43 (L3). In addition, the ribose moiety of A43 (L3) forms two hydrogen bonds with A36 (L3), further stabilizing this layer (Fig. 2e and Extended Data Fig. 3e). At the bottom layer, G23 from J2/3 forms a canonical Watson-Crick base pair with C44 from L3, while G27 (J2/3) pairs with C35 (L3) (Fig. 2f-g and Extended Data Fig. 3f-g). The

bound TMR-DN is located above these three layers, in which the two base triplets located in the middle (G26-A43-A36) and upper (A24-A42-A37) layers establish a robust structural platform that stabilizes the TMR-DN binding pocket, and facilitate the fluorescence activation of the bound fluorophore (Fig. 1f-g and Extended Data Fig. 3b-c).

Mutations to disrupt the formation of the A24-A42-A37 base triplet beneath the fluorophore, as well as G26-A43-A36 supporting the binding pocket, significantly impaired fluorescence activation (Fig. 2h). Specifically, substitutions such as A24C, A42C, G26C, and A43U all reduced fluorescence by over 50% compared to RhoBAST-WT (Fig. 2h). For the two Watson-Crick base pairs below the TMR-DN binding pocket, G23-C44 and G27-C35 (which are formed between J2/3 and L3), we observed that mutating G23 to C caused a dramatic reduction in fluorescence. In contrast, replacing the G23-C44 pair with G-U or A-U pairs resulted in a less severe effect, with the fluorescence reduction being less than 40% (Fig. 2h). Similarly, disrupting the G27-C35 base pair by mutating G27 to C led to low fluorescence, while substituting G27-C35 with G27-U35 or A27-U35 has minimal impact on the fluorescence (Fig. 2h). Notably, replacing U22-A28 within J2/3 with U-U, U-G, or G-C similarly does not significantly affect their ability to activate TMR-DN fluorescence (Fig. 1h and 2h).

Collectively, these results highlight the critical role of long-distance interactions in maintaining the structural integrity and fluorescence activation of the RhoBAST/TMR-DN complex. They underscore the delicate interplay between the binding pocket architecture and distal elements in supporting TMR-DN fluorescence. Based on our structural observation and the mutation analysis, we mapped these long-distance interactions onto the original secondary structure of RhoBAST. With the exception of A25, all nucleotides in J2/3 participate in these interactions (Fig. 2j). These interactions collectively define the RhoBAST scaffold and stabilize the TMR-DN binding pocket at the top terminal of RhoBAST.

Composition of the RhoBAST binding pocket in free and TMR-DN-bound form

As shown in the TMR-DN-bound RhoBAST structure (Fig. 1f-g), the binding pocket is located in the upper region of the structure, formed by J2/3 and L3. The corresponding region in the free-form RhoBAST structure also comprises by J2/3 and L3 (Fig. 1d-e). In the both free-form and TMR-DN-bound form structures, two base triplets A24(J2/3)-A42(L3)-A37(L3) and G26(J2/3)-A43(L3)-A36(L3) are formed between L3 and J2/3, serving as a stable platform that supports the tertiary folding of the binding pocket region (Fig. 1d, 1f, 2c and Extended Data Fig. 3a-c). However, above these two base triplets, the intervening region G38-G39-U40-U41 of L3 adopts different conformation at the top terminal of free-form and bound form structures (Fig. 3).

The surface representation of the top terminal region in the free-form structure reveals a compact structural bump composed of G38-G39-U40-U41, positioned nearly vertically above A24(J2/3)-A42(L3)-A37(L3) base triplet plane (Fig. 3a). Within the bump, G38 intercalates between G39 and the underlying base triplet, forming a continuous stacking interaction that contributes to the structural integrity and spatial organization of the top terminal region (Fig. 3b). U40 protrudes toward the backside of the bump and does not engage in interactions with other nucleotides (Fig. 3c-d). In contrast, U41 extend towards the base side of G38 and G39 above the base triplet plane A24(J2/3)-A42(L3)-A37(L3) and participates in multiple hydrogen-bonding interactions with neighboring nucleotides (Fig. 3c-d). Specifically, N3 of U41 forms a hydrogen bond with N3 of G39, O2 of U41 forms a hydrogen bond with the 6-NH_2 of A24, while U41 interacts with G38 through a *cis* sugar edge-sugar edge pairing, in which the O2 and ring oxygen of U41 each form two hydrogen bonds with the 2-NH_2 and 2'-OH of G38, respectively (Fig. 3c). Through this strategic positioning and multiple hydrogen bonds, U41 plays a central ‘locking’ role by anchoring the top terminal nucleotides above the A24(J2/3)-A42(L3)-A37(L3) base triplet plane, thereby stabilizing a relatively tighter closed state of the binding pocket region in the free-form RhoBAST structure. Notably, while G38 adopts 3'-*endo* sugar pucker, G39, U40 and

U41 in the top terminal region all adopt 2'-*endo* sugar pucker in the free-form structure (Fig. 3d).

In the bound-form structure, the TMR-DN binding pocket is constituted by consecutive residues A37 to A42 from the L3 loop, together with A24 from the J2/3 junction. Surface representation indicates that the binding pocket adopts a distinctive finger-and-palm-like conformation (Fig. 3e), in which the stably formed base triplet A24(J2/3)-A42(L3)-A37(L3) constitutes the palm, providing a structural platform for TMR moiety binding, while G39 and U41 form the fingers that clamp the xanthene moiety of TMR. G38 flips out from the binding pocket and stacks above A37, acting as the thumb, thereby creating sufficient space within the binding pocket to accommodate the entry of TMR-DN (Fig. 3e-f). The interactions between U41(L3) and A24(J2/3), G38(L3), and G39(L3) undergo significant rearrangement upon TMR-DN binding. Specifically, in the TMR-DN-bound state, no hydrogen bonds are formed between U41 and G38. Instead, the O2′ atom (rather than the O2 atom) of U41 forms a hydrogen bond with the 6-NH_2 group of A24. Although the conformation of U41 is altered, its hydrogen bond with G39 is retained. Additionally, a new hydrogen bond is established between the O4 atom of U41 and the N2 atom of G39 (Fig. 3g). The xanthene moiety of TMR-DN is sandwiched between the top base triplet, G38-G39-U41 and the bottom palm base triplet A24-A42-A37, bracketed by the thumb-like G38 within the pocket. At the edge of the binding pocket, the carboxyl oxygen of the benzoic acid moiety forms two hydrogen bonds with Watson-Crick edge of G39 (Fig. 3g). Here, the calculated $2F_{observe}$-$F_{calculate}$ $(2F_o - F_c)$ composite omit map of TMR-DN contoured at 1.0 σ level, is shown in Fig. 3g. From a dorsal perspective of L3 loop, we further observe that the N2 of G38 forms an intra-residue hydrogen bond with its own phosphate oxygen (Fig. 3h). We propose that this interaction may contribute modestly to stabilizing the "open" conformation of G38. Notably, G38, G39, U40, and U41 in the top terminal region all adopt a 2'-*endo* sugar pucker in the bound-form structure. This stacking interaction and the hydrogen bonding interaction between G39 and the TMR segment of TMR-DN not only anchors fluorophore TMR within the binding pocket but also enhances its

stability through additional hydrogen bonding. The stable binding of RhoBAST to the TMR moiety increases the physical distance between the fluorophore TMR and the quencher DN, disrupts the effective quenching distance for contact-quenching, thereby facilitating the activation of fluorescence.

Comparative analysis of RhoBAST binding pocket between free-form and TMR-DN-bound structures

Alignment of the free-form and TMR-DN-bound form RhoBAST structures indicated that L3 loop exhibits significant conformational changes (Fig. 4a and Extended Data Fig. 2a). Compared to the compact top terminal fold spanning G38 to U41 observed in the free-from structure, the corresponding region (G38-G39-U40-U41) in the TMR-DN bound structure, adopts a widened and loosely packed conformation above the base triplet A24(J2/3)-A42(L3)-A37(L3). Within this rearranged architecture, U40 consistently remains flexible and distanced from the central region but shifts from the back toward the front of the terminal loop, while G39 and U41 move closer together, forming hydrogen bonds through G39's Watson-Crick edge and U41's sugar edge (Fig. 3g). Among these nucleotides, G38 exhibits the most pronounced deviation: rather than being sandwiched between A42 and G39 as in the apo form, it flips outward to stack directly on A37. The flipping motion of G38 effectively releases itself from the constraints imposed by U41 in the free-form structure, leading to the formation of a central cavity within the top terminal region and creating sufficient steric space to accommodate TMR-DN binding (Fig. 4b). Consistent with this model, structural superposition revealed that the position of G38 in the free-form structure sterically clashes with the bound TMR moiety, underscoring the necessity of the flipping mechanism for ligand accommodation (Fig. 4b).

Guided by the structural comparative analysis of the top terminal region that forms the TMR-DN binding pocket, we introduced nucleotide substitutions and assessed their ability to activate the fluorescence of TMR-DN *in vitro* (Fig. 4c). As shown in Fig. 4c, single substitutions of U41 to C or A, as well as G39 to A, U, or C, resulted in

negligible fluorescence activation (Fig. 4c). These findings are consistent with the extensive interactions formed between G39 and U41 in both the free and bound structures, highlighting their indispensable role in establishing the binding pocket and enabling fluorescence activation of TMR-DN. In addition to these nucleotides, we also mutated U40 to A/G/C, which showed little effect on the fluorescence activation. This result is consistent with the structural observations that U40 exhibits flexibility in both free-form and bound-form structures (Fig. 3).

Given that nucleotide G38 undergoes the most pronounced conformational change upon TMR-DN binding, we introduced point mutations by substituting G38 with A, U, or C. Unexpectedly, fluorescence assays revealed that replacement of G38 with either U or C completely abolished fluorescence activation, whereas the G38A mutant retained comparable activity to the wild-type (Fig. 4c). This result indicates that the presence of a purine at position 38 may be essential for maintaining an optimal binding geometry and efficient fluorescence activation.

To further characterize the intrinsic molecular properties supporting super-resolution imaging and compare the involved interactions between RhoBAST variants (wild-type and G38A) and the fluorogenic dye TMR-DN during the fluorescence activation, we performed surface plasmon resonance (SPR) assays to quantify the binding kinetics and affinities independently of using fluorescence measurements. Both the wild-type and G38A mutant RNAs exhibited robust binding to TMR-DN. Equilibrium dissociation constants (K_d) were determined to be 133 nM and 219 nM for the wild-type and G38A, respectively. Kinetic analysis yielded association rate constants (*k_on*) of 6.54×10^5 $M^{-1}s^{-1}$ and 1.00×10^5 $M^{-1}s^{-1}$, and dissociation rate constants (*k_off*) of 8.72×10^{-2} s^{-1} and 2.19×10^{-2} s^{-1} for the wild-type and G38A, respectively (Fig. 4d and 4e). G38A mutant exhibits moderately slower association and dissociation kinetics, suggesting that the guanine-to-adenine replacement subtly perturbs local stacking or hydrogen-bonding interactions that stabilize the ligand-binding pocket. Nevertheless, the overall affinity and fluorescence activation remain largely preserved, indicating that the presence of a purine at position 38 maintains the

structural integrity required for efficient ligand recognition and signal transduction.

Mechanistic insights from computational and structural analyses of RhoBAST mutants and ligand complexes

To explore the structural role of residue 38 in ligand recognition and folding stability, we conducted computational mutagenesis based on the complex structure of RhoBAST bound with TMR-DN. Residue 38 was systematically substituted with each of the four nucleobases (A, U, G, or C), while keeping all other positions fixed, followed by local re-optimization of the base coordinates of residue 38 and the backbone atoms of residues 37-39 (Extended Data Fig. 4a). BRIQ folding energy calculations revealed that the G38 and A38 variants respectively have average folding energies -352.8 kcal/mol and -351.8 kcal/mol, while those of the U38 and C38 variants are -348.3 kcal/mol and -348.6 kcal/mol, respectively (Extended Data Fig. 4b). Among these variants, the energetic preference of the A38 mutant stems from adenine-adenine stacking, while that of the G38 mutant arises from adenine-guanine stacking as well as hydrogen bonding between G38 and the backbone phosphate. Both variants stabilize the local binding pocket architecture and facilitate efficient fluorophore accommodation, thereby activating fluorescence.

To further gain the underlying mechanism from a structural perspective, we determined the crystal structures of the G38A and G38U mutants in their ligand-free states (Fig. 5a and Extended Data Fig. 5a) and the G38A mutant, which retains fluorescence activation ability, in its TMR-DN bound state (Fig. 5b). As shown in Fig. 5c, comparison of the wild-type, G38A, and G38U structures demonstrated that their global architectures are broadly similar. Nonetheless, the top terminal region ranging from (G/A/U)38 to U41 of the three structures each adopt distinct conformations, indicating its intrinsic flexibility in the free state. This observation was further supported by their respective structural B-factor analysis, which indicated elevated flexibility in these regions (Extended Data Fig. 5b-d). In the complex structure of the G38A mutant bound with TMR-DN, TMR-DN is also encapsulated by the top terminal of G38A mutant

structure (Fig.5b and Extended Data Fig. 6a-c). Structural comparison indicates that the bound structure of G38A closely resembled that of the wild-type TMR-DN-bound complex, with the exception of U40, which remains relatively flexible (Fig. 5d and Extended Data Fig. 6d-e). Apart from this minor local conformation variation, all other nucleotides adopted nearly identical conformations. In the G38A complex structure, A38 flips outwards and stacks above A37 as well (Extended Data Fig. 6a-c), therefore preserving the characteristic cavity architecture of the binding site observed in the wild-type complex structure and leaving sufficient space for fluorophore accommodation. Structural comparison of the G38A mutant in its free and TMR-DN-bound states reveals a nucleotide flipping motion at position 38 as well (Fig. 5e and Extended Data Fig.7a-b), reflecting an intrinsic conformational adaptability that underlies RhoBAST's fluorogenic activation process.

Alignment of TMR-DN-bound complex structures of wild-type RhoBAST, the G38A variant and the previously reported RhoBAST variant (termed Add-UA) containing an addition U1A loop (PDB: 8JY0)[21], revealed that the TMR moiety are consistently positioned within the binding pocket across all structures (Extended Data Fig.8a-d). In contrast, the DN moiety exhibits positional variability and adopts distinct conformations (Extended Data Fig.8a-d), suggesting greater structural flexibility in this region. To further dissect the contribution of different moieties of TMR-DN to binding, SPR assays were also performed to quantify the kinetic and equilibrium binding parameters of wild-type RhoBAST with 5-TAMRA and TMR, in which the DN moiety is replaced by -COOH or deleted, respectively (Extended Data Fig. 9a). Both 5-TAMRA and TMR displayed comparable binding affinities to TMR-DN, with equilibrium dissociation constants (K_d) of 68.6 nM and 58.3 nM, association rate constants (*k_on*) of 4.40 × 10^5 $M^{-1}s^{-1}$ and 3.85 × 10^5 $M^{-1}s^{-1}$, and dissociation rate constants (*k_off*) of 3.02 × 10^{-2} s^{-1} and 2.05 × 10^{-2} s^{-1}, respectively (Extended Data Fig. 9b-c). These results indicate that fluorescence activation of TMR-DN by RhoBAST primarily arises from recognition and binding of the TMR core fluorophore rather than interactions involving the DN moiety. Further structural determination of RhoBAST in complex with TMR and 5-TAMRA

revealed that both complexes adopt highly similar overall conformations to that of the TMR-DN–bound structure (Extended Data Fig. 9d-e), with structural superimpositions yielding low RMSD values of 1.098 Å and 0.673 Å, respectively (Extended Data Fig.10a-b). They share identical pocket compositions, with residue G38 adopting a splayed-out conformation across different bound states (Extended Data Fig.10c-e), suggesting a conserved role of G38 in preserving the fluorophore-binding geometry and facilitating fluorescence activation.

Insights on ligand-induced RNA conformational changes by 2-aminopurine fluorescence experiments

To evaluate ligand-induced conformational changes at the binding site of the RhoBAST aptamer, we used a fluorescence spectroscopic approach relying on RhoBAST aptamer variants with 2-aminopurine (Ap) substitutions of individual nucleobases (Fig. 6a). This approach also enables estimation of ligand binding thermodynamics and kinetics[22,23]. Guided by the comparison of the free and ligand-bound RhoBAST structures, we selected two nucleoside positions (G38 and U40) within the binding pocket for the single 2-aminopurine substitution that we considered likely to undergo conformational changes in response to ligand addition (Fig. 6a, b). Accordingly, we synthesize two truncated constructs in which one base pair in stem P1 was deleted, and G38 and U40 was individually replaced with Ap (Fig. 6a). For clarity and consistency, nucleotide numbering was maintained as shown in Fig. 1b.

As shown in Fig. 6b and Fig. 3b, G38 is sandwiched between A42 and G39 in the ligand-free state, whereas in the ligand-bound state it is displaced by TMR moiety and flips outwards to stack above A37. In the G38Ap RNA assay, this conformational rearrangement is accompanied by fluorescence quenching upon ligand binding (Fig. 6c). U40 points outwards and is unstacked in the ligand-free state, but becomes stacked atop U41 in the ligand-bound state. As expected, a decrease in fluorescence is observed for the U40Ap RNA in response to the addition of 5-TAMRA (Fig. 6d). These results demonstrate that the conformational transitions of G38 and U40 can be

effectively monitored by 2-aminopurine fluorescence, providing direct evidence of local structural rearrangements, and, in particular, the specific nucleotide motions that occur during ligand binding. The concentration-dependent fluorescence changes of the G38Ap and U40Ap variants yielded apparent dissociation constants (K_d) of 0.18 ± 0.01 μM and 0.34 ± 0.03 μM, respectively, in good agreement with with K_d values obtained by our previous SPR experiments (Fig. 6d, f).

To further investigate the relationship between the flipping motion of the G38Ap nucleotide and the ensemble conformational dynamics of the RhoBAST aptamer, we monitored 5-TAMRA binding in real time using the fluorescence signal of the G38Ap variant. This approach allowed us to directly probe the kinetics of this purine nucleotide during the ligand-capturing process, yielding an observed rate constant of k_{obs} = 0.68 ± 0.09 s^{-1} at the 5-TAMRA concentration of 1 μM (Fig. 6g). Notably, this value aligns closely with the k_{obs} = 0.65 s^{-1} calculated from the association rate constant (k_on = 6.54 × 10^5 $M^{-1}s^{-1}$) of WT-RhoBAST determined by SPR experiments at the same TMR concentration (Fig. 4d-e). These results also suggest that spontaneous transient flipping of G38 allows for the initial ligand-capturing event of RhoBAST through a *conformational selection* process (reflected in k_{obs} of G38Ap), followed by further RNA conformational adaptions according to an *induced fit* process[24,25]. These adaptions are usually slower[26], and indeed, we observed an 8-fold slower rate for U40Ap (k_{obs} = 0.0848 ± 0.002 s^{-1} at the 5-TAMRA concentration of 1 μM; Fig. 6h). Both processes contribute to the overall aptamer dynamics and efficient fluorophore engagement.

Together, we propose a mechanistic model for ligand recognition and fluorescence activation in RhoBAST (Fig. 6i). In the free-state, G38 is stacked directly on the base-triple platform, forming a compact yet flexible terminal structure that lacks a defined binding cavity for the fluorophore. G38 undergoes spontaneous outward flipping events, and thereby relocates to the side of the platform allowing for initial TMR contacts. G38 itself becomes stabilized through π-π stacking interactions with A37.The intrinsic flexibility of the terminal region in the free-form aptamer lowers the energetic barrier for ligand entry and enables a rapid binding rate, while also facilitating the

conformational rearrangement of G38. Once the ligand is accommodated, the stable stacking between G38 and A37 helps to lock the aptamer in the bound state, stabilizing the fluorophore and promoting fluorescence activation. This nucleotide-flipping mechanism, observed here for the first time in a fluorogenic RNA aptamer, highlights a dynamic strategy by which aptamers can couple local nucleotide conformational transitions to global ligand recognition. It provides a structural and mechanistic blueprint for the rational design of next-generation super-resolution RNA imaging aptamers with enhanced binding kinetics, fluorescence efficiency, and structural adaptability.

Discussion

Fluorescent light-up aptamers (FLAPs) have become powerful tools for RNA detection and imaging in living cells[27]. Among these, RhoBAST excels in super-resolution RNA imaging due to its exceptional performance[17]. Our determination of the first free-form structure of the fluorogenic RNA aptamer RhoBAST provides an unprecedented glimpse into the early molecular events governing ligand recognition and fluorescence activation. In this unbound conformation, the terminal region adopts a compact yet flexible architecture in which G38 stacks directly atop the base-triple platform, creating a closed conformation devoid of a binding cavity. The flexibility endows the terminal domain with intrinsic adaptability, enabling rapid ligand access and efficient structural rearrangement upon binding. Upon fluorophore binding, this region undergoes a remarkable transformation: The local, inherent conformational dynamics of G38, in form of transient flips, enables the initial contact between the platform and the fluorophore. Thereby, G38 relocates to its side while maintaining π-π stacking stabilization with A37. This outward flipping motion, identified here for the first time in a fluorogenic RNA aptamer, establishes a direct mechanistic link between local nucleotide dynamics and global ligand recognition. Kinetic analyses using 2-aminopurine substitution and surface plasmon resonance (SPR) demonstrate that this conformational switch facilitates rapid ligand capture and low activation energy, underpinning the transient “flickering” fluorescence behavior essential for super-

resolution imaging.

Historically, structural studies of fluorogenic RNA aptamers[28-31], as well as other regulatory RNA molecules such as riboswitches[32-34], have focused almost exclusively on their ligand-bound states, which depict the stabilized binding pocket and the specific ligand or fluorophore interactions that define the activated conformation. While these structures have been invaluable for understanding the final, active conformations of aptamers, they offer only a static view of the binding process and provide limited information about the conformational dynamics that precede ligand engagement. Only a handful of studies have captured unbound, or free-form RNA conformations—and even in those rare cases, the unbound structures typically closely resemble their bound counterparts[35,36]. By contrast, the RhoBAST free-form structure reveals both global similarity and pronounced local divergence, particularly at the terminal region where the G38 orientation differs markedly between states. This distinction underscores that fluorescence activation is not merely a static binding event, but a dynamic, multi-step process driven by conformational flexibility and localized nucleotide motion. The elucidation of this free-form state therefore fills a crucial gap in understanding the molecular mechanism that enables fluorogenic activation and defines how structural plasticity couples with ligand kinetics. By resolving this long-missing structural snapshot, our study demonstrates that intrinsic flexibility within the aptamer scaffold is not a liability but a design feature, finely tuned to balance structural stability with dynamic responsiveness.

Fluorogenic RNA aptamers represent powerful molecular tools for visualizing and probing RNA dynamics in living cells. With the rapid advancement of artificial intelligence-driven molecular design, the intelligent engineering of RNA molecules is becoming increasingly feasible[37]. Our structural and mechanistic elucidation of RhoBAST provides a critical reference framework for the AI-guided design and optimization of next-generation super-resolution RNA aptamers with enhanced brightness, stability, and dynamic performance. These mechanistic insights offer a powerful blueprint for the rational design of next-generation super-resolution RNA

aptamers. The identification of one nucleotide (G38) flipping mechanism provides a generalizable strategy to enhance ligand accessibility and fine-tune binding kinetics, while the modular architecture revealed in both free and bound states offers a blueprint for sequence optimization to improve fluorescence efficiency, brightness, and photostability. Guided by this framework, future engineering efforts may exploit controlled nucleotide flexibility and engineered stacking interfaces to achieve faster ligand exchange, reduced off-target interactions, and superior photophysical properties under cellular conditions.

Methods

RNA preparation

To facilitate the crystallization of the RhoBAST/TMR-DN complex, several modifications were introduced, including stable tetraloops (GNRA and UNCG) and the U1A protein-binding loop, to replace the variable loop of stem P2 in our RNA constructs. The target RNA sequences, followed with the HDV ribozyme for self-cleavage, were cloned into the pUT7 plasmid under the control of T7 promoter. These plasmids were amplified in *E. coli* and subsequently linearized using *Hin*d III restriction endonuclease to generate the DNA template necessary for transcription. *In vitro* transcription was carried out at 37°C for 4 hours using T7 RNA polymerase, followed by RNA purification via urea-denaturing polyacrylamide gel electrophoresis (PAGE). RNA products were visualized under UV light, excised from the gel, and extracted into 0.5× Tris-acetate-EDTA (TAE) buffer. The RNA was then precipitated with isopropanol, washed with 80% ethanol, and lyophilized before being dissolved in diethyl pyrocarbonate (DEPC)-treated double-distilled water. The prepared RNA was subsequently used for annealing and crystallization experiments with the ligand TMR.

Ligands

TMR-DN was synthesized and purified following the procedures described in the referenced literature[38]. In brief, the synthesis begins with the reaction of

dinitrofluorobenzene with 2,2'-(ethylenedioxy) bisethylenediamine to produce the intermediate product DN-PEG_3-Amine (DPA). The intermediate is then reacted with 5-carboxy-tetramethylrhodamine-N-hydroxysuccinimide at room temperature. The product is then purified using a reverse phase C-18 column (60% acetonitrile, 0.1% trifluoroacetic acid) to ultimately yield the pure TMR-DN. Tetramethylrhodamine (TMR) was purchased from Zhengzhou Alfachem Co., Ltd. 5-TAMRA was purchased from Beijing Okeanos Technology Co., Ltd.

Crystallization

RNA crystallization was carried out using the sitting-drop vapor diffusion method at 16 °C, with RNA samples and reservoir solution mixed in a 1:1 ratio. RNA samples with modified termini were prepared at 0.4 mM in a buffer containing 50 mM HEPES (pH 7.4), 125 mM KCl, and 5 mM $MgCl_2$. The samples were then annealed at 65 °C for 5 minutes and cooled on ice for at least 30 minutes. For the RhoBAST complex, fluorophore was added to the RNA solution at a final concentration of 2 mM and incubated on ice for an additional hour. High-resolution crystals of RhoBAST in TMR-DN bound form were obtained after three days under conditions of 0.2 M Magnesium acetate tetrahydrate, 0.1 M sodium cacodylate trihydrate pH 6.5 and 30% v/v MPD. Crystals in free form grew under conditions contains 0.2 M NaCl, 0.1 M Na/K phosphate pH 6.2, 40% PEG 400. Crystals of RhoBAST/TMR complex grew under conditions contains 0.01 M $MgCl_2$, 0.05 M sodium cacodylate trihydrate pH 6.5 and 1.9-2.3 M $(NH_4)_2SO_4$. Crystals of free-form RhoBAST-G38A grew under conditions contains 1 M NaCl, 0.1 M odium cacodylate trihydrate pH 6.5, 30% PEG 600, 10% glycerol. Crystals of RhoBAST-G38A/TMR-DN complex grew under conditions contains 2 M $(NH_4)_2SO_4$, 5% 2-Propanol. Crystals of free-form RhoBAST-G38U grew under conditions contains 2 M $(NH_4)_2SO_4$, 0.1 M HEPES pH 7.5, 45% MPD. All crystals were flash-frozen in liquid nitrogen prior to X-ray diffraction data collection. For anomalous diffraction data collection, crystals were quickly soaked in their respective crystallization conditions supplemented with 0.2 M selenourea.

Structure determination and refinement

The X-ray crystallography diffraction data were collected at beamline BL02U1, BL18U1 and BL19U1 at the Shanghai Synchrotron Radiation Facility (SSRF). The raw data were processed with autoPROC [39] and HKL3000 (HKL Research). The structural phase of the RhoBAST-TMR complex was resolved using the AutoSol program in the Phenix suite, employing single-wavelength anomalous diffraction (SAD) based on selenium (Se) anomalous signals(Supplementary Fig. 1) [40]. The initial phases for the free-form RhoBAST-WT and G38A and their other fluorophore complexes were solved by molecular replacement in Phenix, with partial RhoBAST/TMR structure serving as the search model. Iterative rounds of model building and refinement were performed using the Phenix suite and Coot software[40-42]. The initial structural model underwent refinement through phenix.refine and was subsequently manually adjusted in Coot. The ligand was incorporated during the final rounds of structure construction and refinement. The X-ray diffraction statistics and structure refinement are provided in Supplementary Table 1-3.

Fluorescence assay and 3D spectroscopy

To validate our observations in the tertiary structure of the RhoBAST/TMR-DN complex, structure-based mutants of RhoBAST aptamer were prepared through *in vitro* transcription. Both RhoBAST wild-type (WT) and its mutants were prepared in ASBT buffer containing 20 mM HEPES at pH 7.4, 125 mM KCl, 5 mM $MgCl_2$, and 0.05% Tween 20. The RNA samples were annealed at 65°C for 5 minutes, followed by cooling on ice for 30 minutes. To evaluate the ability of RhoBAST mutants to activate the fluorogenic ligand TMR-DN, a mixture of 0.1 μM TMR-DN and 0.5 μM annealed RNA was incubated at room temperature for 30 minutes before fluorescence measurements. Fluorescence measurements were conducted using Shimadzu RF-6000 spectrofluorophotometer set to an excitation wavelength of 563 nm and an emission wavelength of 587 nm. Each fluorescence experiment was independently repeated three times to ensure reproducibility. Three-dimensional fluorescence spectra of

RhoBAST and its mutants in complex with TMR-DN (5 μM RNA and 3 μM TMR-DN) were also measured using the same instrument. The excitation wavelength range was set to 400-700 nm, and the emission range to 500-800 nm, with a 5 nm data interval and a scanning speed of 12000 nm/min. Data analysis and visualization were carried out using OriginPro and GraphPad Prism software.

Surface plasmon resonance (SPR) measurements

Surface plasmon resonance (SPR) measurements were performed on a Biacore 1K+ system (GE Healthcare) maintained at 25°C throughout the analysis. The running buffer ASBT consisted of 20 mM HEPES-K pH 7.4, 125 mM KCl, 5 mM $MgCl_2$ and 0.05% (v/v) Tween-20. A streptavidin-coated SA sensor chip (GE Healthcare) was employed for ligand immobilization: 5′-biotinylated RhoBAST WT or G38A RNA (100 ng/μL) was captured until a final immobilization level of about 2500 response units (RU) was achieved. Analytes (TMR-DN, 5-TAMRA, TMR) were introduced in duplicate two-fold dilution series (4 μM–7.81 nM) at 30 μL min^{-1}, allowing 120 s for association, followed by 150 s dissociation in ASBT supplemented with 1% (v/v) DMSO, solvent correction was also conducted. Sensorgrams were processed with Biacore Insight Evaluation software; bulk refractive-index contributions were removed by subtracting the response from the reference flow cell and an average of buffer-only injections.

2-Aminopurine Fluorescence spectroscopy

All steady-state fluorescence spectroscopic experiments were measured on a Cary Eclipse spectrometer (Varian, Australia) equipped with a peltier block, a magnetic stir-ring device and a RX2000 stopped-flow apparatus (Applied Photophysics Ltd., UK). The data obtained were processed with OriginPro 2018 software (OriginLab, USA). Aminopurine-modified RNA samples were prepared in 0.5 μM concentration in a total volume of 120 μl (qualitative analysis) or 1 ml (quantitative analysis) of buffer (50 mM MOPS, 100 mM KCl, pH 7.5 (25°C)). The samples were heated to 90°C for 2 min, allowed to cool to room temperature, transferred to quartz cuvettes equipped with a small stir bar and held at 20°C in the Peltier controlled sample holder. Then, ligands

were manually pipetted in a way not to exceed a total volume increase of 3%. The solution was stirred after ligand addition and allowed to equilibrate for at least 15 min before data collection. Spectra were recorded from 320 to 500 nm using the following instrumental parameters: excitation wavelength, 308 nm; increments, 1 nm; scan rate, 120 nm min^{-1}; slit widths, 10 nm. Thermodynamic and kinetic parameters K_d and k_{obs} were obtained as described in reference[43].

Data availability

The atomic coordinates and structure factors have been deposited to the Protein Data bank (www.rcsb.org) under the following accession codes: 9XAL for the RhoBAST-WT/TMR-DN complex, 9X9O for the free-form RhoBAST-WT, 9XAN for the free-form G38A,9XAL for the RhoBAST-G38A/TMR-DN complex, 9XAQ for free-form RhoBAST-G38U, 9L8F for the RhoBAST-WT/TMR complex crystals soaked with selenourea, 9X9N for the RhoBAST-WT/5-TAMRA complex. All study data are included in the article and Supplementary Materials.

Acknowledgments

We thank the staff members of the Large-scale Protein Preparation System, BL-17B, BL-17U1, BL18U1, BL-19U1 and BL02U1 beamlines at the National Facility for Protein Science in Shanghai (NFPS), Zhangjiang Lab, China for providing technical support and assistance in data collection and analysis. We thank the staff of the BL02U1 beamline at the National Center for Protein Sciences Shanghai (NCPSS) at SSRF for their assistance in X-ray data collection. We thank the technical assistance from the core facility of the Life Sciences Institute (LSI), Zhejiang University. This work was supported by the National Natural Science Foundation of China [32325029, 91940302, and 91640104 to A.R.], the National Key Research and Development Project of China [2023YFC2604300 to A.R.], the major program of Zhejiang Province [LD25C050002 to A.R.].

Author contributions

X.T. and M.H. undertook all crystallographic experiments and collected the diffraction data with the assistance of Z.H., X.B. and H.Y. under the supervision of A.R. The structures were solved by X.T., M.H. and A.R. and analyzed by A.R. and J.Z. with the help of P.X., X.S., H.L. and Y.L. X.T., C.M. performed substitutions and functional assays with the help of M.H. and Z.H. under the supervision of A.R. and J.Z. The paper was written jointly by A.R., J.Z. and R.M. with input from the remaining authors.

Competing interests

The authors declare no competing interests.

Figure Captions

Figure 1 | Secondary and tertiary structure of free-form and TMR-DN-bound RhoBAST. **a**, Chemical structure of the fluorophore tetramethylrhodamine (TMR) conjugated with the quenching group dinitroaniline (DN). **b**, The secondary structure of wild-type (WT) RhoBAST used in structural determination. **c**, The three-dimensional fluorescence spectra of TMR-DN in the absence (upper panel) and presence (lower panel) of RhoBAST. In the absence of RhoBAST, TMR-DN exhibited a maximum excitation wavelength of 555 nm and a maximum emission wavelength of 585 nm. While in the presence of RhoBAST-WT, the spectra showed a redshift, with excitation and emission wavelengths shifting to 565 nm and 590 nm, respectively, along with a significant fluorescence intensity increase. **d-e**, Schematic representation (**d**) and cartoon representation (**e**) of the tertiary structure of free-form RhoBAST. **f-g**, Schematic representation (**f**) and cartoon representation (**g**) of the tertiary structure of TMR-DN-bound RhoBAST. Same color code is used in the schematic representation and cartoon representation. **h**, Terminal residues of J2/3, U22 and A28 form a canonical Watson-Crick base pair. **i**, Two hydrogen bonds—between A28 and C8, G29 and U7—further stabilize the base-pair stacking interactions, and bridge two coaxial helixes (P2 with J2/3 and P1 with P3).

Figure 2 | Long-range interactions of free-form RhoBAST. a, Complete schematic representation of free-form RhoBAST. Nucleotides outlined in gray denote bases that adopt similar conformations in both the free and TMR-DN-bound forms. **b**, Cartoon representation of the tertiary structure of free-form RhoBAST, with nucleotides involved in long-range interactions highlighted in stick represetation. **c**, Structural organization of the interactions between junction J2/3 and terminal loop L3, with nucleotides involved in long-range interactions highlighted in stick represetation. **d-g**, Close-up view of the base triple A24(J2/3)-A37(L3)-A42(L3) (**d**), G26 (J2/3)-A43 (L3)-A36 (L3) (**e**), canonical Watson–Crick base pairs G23(J2/3)-C44(L3) (**f**), G27(J2/3)-C35(L3) (**g**). **h**, *In vitro* fluorescence assay of the mutants of RhoBAST aptamer (nucleotides involved in long-range interactions). The fluorescence intensity of TMR-DN activated

by RhoBAST mutants from three independently repeated experiments are normalized for comparison with the RhoBAST-WT aptamer. Data represent the mean ± s.d. from three replicates. **j**, The secondary structure of RhoBAST, with long-distance interactions denoted by dotted lines. Red dotted lines represent the Watson-Crick base pair, while black dotted lines indicate non-canonical base pairs.

Figure 3 | Detailed comparison of the top terminal region between the free and TMR-DN-bound RhoBAST. a, Surface representation of the top terminal region of free-form RhoBAST, which adopts a compact vertical conformation. **b**, Cartoon and stick representation of the top terminal region of free-form RhoBAST. **c**, Close-up view of the top terminal region of free-form RhoBAST. U41 forms hydrogen bonds with N3 of G39, 6-NH_2 of A24, 2-NH_2 and 2'-OH of G38, respectively. **d**, Dorsal perspective of the top terminal region of free-form RhoBAST. G38 adopts 3′-*endo* sugar pucker, whereas G39, U40 and U41 adopt 2′-*endo* conformation. **e**, Surface representation of the RhoBAST aptamer bound to TMR-DN (shown in spheres). The binding pocket adopts a distinctive finger-and-palm-like conformation. The TMR moiety of TMR-DN is clamped by J2/3 and L3 loops, leaving its DN tail exposed beyond the pocket. **f**, Cartoon and stick representation of the binding pocket of RhoBAST/TMR-DN complex, with TMR-DN shown in surface. **g**, Close-up view of the top base triple G38-G39-U41. The sugar edge of G39 forms two hydrogen bonds with the Watson-Crick edge of U41, while O2’ of U41 interacts with the N6 of A24. The carboxyl oxygen of TMR moiety forms two hydrogen bonds with Watson-Crick edge of G39 in the top triple. The $2F_{observe}$-$F_{calculate}$ $(2F_o - F_c)$ composite omit map of TMR-DN contoured at level 1.0 σ is shown. **h**, Dorsal perspective of L3 of RhoBAST/TMR-DN complex. The N2 of G38 forms an intra-residue hydrogen bond with its own phosphate oxygen.

Figure 4 | Comparative structural analysis of the RhoBAST binding pocket in its ligand-free and TMR-DN-bound states. a, Alignment of L3 region between free-form (mainly green) and TMR-DN-bound (gray) RhoBAST, G38 exhibits the most pronounced deviation. **b**, Surface representation of the RhoBAST bound to TMR-DN (shown in spheres), both free-form and TMR-DN-bound RNA’s cartoon representation

of the top terminal region is shown at the same time, with G38 highlighted in stick rendering. **c**, *In vitro* fluorescence assay of the mutants of RhoBAST aptamer (nucleotides involved in binding pocket). The fluorescence intensity of TMR-DN activated by RhoBAST mutants from three independently repeated experiments are normalized for comparison with the RhoBAST-WT aptamer. Data represent the mean ± s.d. from three replicates. **d-e**, SPR experiment of RhoBAST-WT (**d**) and RhoBAST-G38A (**e**) binding with TMR-DN.

Figure 5 | Structure organization of RhoBAST G38 mutants. a-b, Cartoon representation of the tertiary structure of RhoBAST G38A mutant in the free-form (**a**) and TMR-DN (shown in spheres)-bound form (**b**). **c**, Overall alignment of the tertiary free-form structures between RhoBAST-WT (colorful), RhoBAST-G38A (slate), and RhoBAST-G38U (gray), with top terminal region shown as surface and stick. **d**, Alignment of the binding pocket between complexes of RhoBAST-WT/TMR-DN (green) and RhoBAST-G38A/TMR-DN (slate). G38 and A38 exhibit the same outward flipping, while U40 maintains its flexibility. **e**, Alignment of the terminal loop region between free-form (slate) and TMR-DN-bound form(gray) structures of RhoBAST G38A mutant. Similar to the flipping of G38 in WT RhoBAST, A38 also undergoes outward flipping events upon TMR-DN binding in RhoBAST G38A mutant.

Figure 6 | Ligand-induced conformational changes revealed by 2-aminopurine fluorescence experiments. a, Secondary structure of RhoBAST aptamer construct used in 2-aminopurine (2-Ap) fluorescence experiments (one base pair A-U in stem P1 was deleted), with the chemical structure of 2-Ap shown below. Two positions for the single 2-Ap substitution are highlighted in red. **b**, Structural modulation of RhoBAST induced by Mg^{2+} and TMR-DN. The color code is same as panel **a**. **c-f**, Real-time fluorescence assay for RhoBAST-G38Ap (**c**) and RhoBAST-U40Ap (**e**) upon sequential addition of Mg^{2+} and ligand (5-TAMRA). Concentration-dependent fluorescence changes of G38Ap (**d**) and U40Ap (**f**) RNA are shown; the normalized fluorescence intensity of the G38Ap (**d**) and U40Ap (**f**) are plotted as a function of RNA concentration. The graphs show the best fit of the two-parametric quadratic fit. The

obtained K_d values for G38Ap (**d**) and U40Ap (**f**) in 50 mM MOPS, 100 mM KCl, pH 7.5, at 293 K, are indicated. Inset: fluorescence emission spectra (λ_{ex} = 308 nm) from 320 to 480 nm of the G38Ap (**d**) and U40Ap (**f**) at each 5-TAMRA concentration. **g-h**, Monitoring the fluorescence signal of G38Ap (**g**) and U40Ap (**h**) RNA after addition of 5-TAMRA (1 μM). The K_{obs} values for G38Ap (**g**) and U40Ap (**h**) are indicated. **i**, Mechanistic model for ligand recognition and fluorescence activation in RhoBAST. Rectangular blocks denote residues involved in long-range interactions; stems are depicted as cylinders. Same color code is used as in the previous figure.

References

1 Pan, Y.-H. *et al.* Pre-rRNA spatial distribution and functional organization of the nucleolus. *Nature*, doi:10.1038/s41586-025-09412-1 (2025).

2 Liu, X. Q. *et al.* De novo assembly of nuclear stress bodies rearranges and enhances NFIL3 to restrain acute inflammatory responses. *Cell* **188**, 4586-4603.e4531, doi:10.1016/j.cell.2025.05.003 (2025).

3 Glotzer, J. B., Saffrich, R., Glotzer, M. & Ephrussi, A. Cytoplasmic flows localize injected oskar RNA in Drosophila oocytes. *Curr Biol* **7**, 326-337, doi:10.1016/s0960-9822(06)00156-4 (1997).

4 Le, P., Ahmed, N. & Yeo, G. W. Illuminating RNA biology through imaging. *Nat Cell Biol* **24**, 815-824, doi:10.1038/s41556-022-00933-9 (2022).

5 Bertrand, E. *et al.* Localization of ASH1 mRNA particles in living yeast. *Mol Cell* **2**, 437-445, doi:10.1016/s1097-2765(00)80143-4 (1998).

6 Larson, D. R., Zenklusen, D., Wu, B., Chao, J. A. & Singer, R. H. Real-time observation of transcription initiation and elongation on an endogenous yeast gene. *Science* **332**, 475-478, doi:10.1126/science.1202142 (2011).

7 Daigle, N. & Ellenberg, J. LambdaN-GFP: an RNA reporter system for live-cell imaging. *Nat Methods* **4**, 633-636, doi:10.1038/nmeth1065 (2007).

8 Yang, L. Z. *et al.* Dynamic Imaging of RNA in Living Cells by CRISPR-Cas13 Systems. *Mol Cell* **76**, 981-997 e987, doi:10.1016/j.molcel.2019.10.024 (2019).

9 Zhou, H. & Zhang, S. Recent Development of Fluorescent Light-Up RNA Aptamers. *Crit Rev Anal Chem* **52**, 1644-1661, doi:10.1080/10408347.2021.1907735 (2022).

10 Paige, J. S., Wu, K. Y. & Jaffrey, S. R. RNA mimics of green fluorescent protein. *Science* **333**, 642-646, doi:10.1126/science.1207339 (2011).

11 Li, X., Kim, H., Litke, J. L., Wu, J. & Jaffrey, S. R. Fluorophore-Promoted RNA Folding and Photostability Enables Imaging of Single Broccoli-Tagged mRNAs in Live Mammalian Cells. *Angew Chem Int Ed Engl* **59**, 4511-4518, doi:10.1002/anie.201914576 (2020).

12 Dolgosheina, E. V. *et al.* RNA mango aptamer-fluorophore: a bright, high-affinity complex for RNA labeling and tracking. *ACS Chem Biol* **9**, 2412-2420, doi:10.1021/cb500499x (2014).

13 Song, W. *et al.* Imaging RNA polymerase III transcription using a photostable RNA-fluorophore complex. *Nature chemical biology* **13**, 1187-1194, doi:10.1038/nchembio.2477 (2017).

14 Chen, X. *et al.* Visualizing RNA dynamics in live cells with bright and stable fluorescent RNAs. *Nature biotechnology* **37**, 1287-1293, doi:10.1038/s41587-019-0249-1 (2019).

15 Jiang, L. *et al.* Large Stokes shift fluorescent RNAs for dual-emission fluorescence and bioluminescence imaging in live cells. *Nature methods* **20**, 1563-1572, doi:10.1038/s41592-023-01997-7 (2023).

16 Buhler, B. & Sunbul, M. Single-Molecule RNA Imaging in Live Cells with an Avidity-Based Fluorescent Light-Up Aptamer biRhoBAST. *Methods Mol Biol* **2822**, 87-100, doi:10.1007/978-1-0716-3918-4_8 (2024).

17 Sunbul, M. *et al.* Super-resolution RNA imaging using a rhodamine-binding aptamer with fast exchange kinetics. *Nat Biotechnol* **39**, 686-690, doi:10.1038/s41587-020-00794-3 (2021).

18 Zhou, X., Gao, H., Xiang, L., Liu, H. & Zhou, X. Developments of the mDZ-RhoBAST Probe for Super-Resolution Imaging of FTO Demethylation in Live Cells. *J Am Chem Soc* **147**, 15732-15739, doi:10.1021/jacs.5c03149 (2025).

19 Buhler, B. *et al.* Avidity-based bright and photostable light-up aptamers for single-molecule mRNA imaging. *Nat Chem Biol* **19**, 478-487, doi:10.1038/s41589-022-01228-8 (2023).

20 Englert, D. *et al.* Fast-exchanging spirocyclic rhodamine probes for aptamer-based super-resolution RNA imaging. *Nat Commun* **14**, 3879, doi:10.1038/s41467-023-39611-1 (2023).

21 Zhang, Y. *et al.* Structural mechanisms for binding and activation of a contact-quenched fluorophore by RhoBAST. *Nature Communications* **15**, doi:10.1038/s41467-024-48478-9 (2024).

22 Haller, A., Soulière, M. F. & Micura, R. The Dynamic Nature of RNA as Key to Understanding Riboswitch Mechanisms. *Accounts of chemical research* **44**, 1339-1348, doi:10.1021/ar200035g (2011).

23 Souliere, M. F., Haller, A., Rieder, R. & Micura, R. A powerful approach for the selection of 2-aminopurine substitution sites to investigate RNA folding. *Journal of the American Chemical Society* **133**, 16161-16167, doi:10.1021/ja2063583 (2011).

24 Bucher, D., Grant, B. J. & McCammon, J. A. Induced Fit or Conformational Selection? The Role of the Semi-closed State in the Maltose Binding Protein. *Biochemistry* **50**, 10530-10539, doi:10.1021/bi201481a (2011).

25 Vogt, A. D. & Di Cera, E. Conformational Selection or Induced Fit? A Critical Appraisal of the Kinetic Mechanism. *Biochemistry* **51**, 5894-5902, doi:10.1021/bi3006913 (2012).

26 Frener, M. & Micura, R. Conformational Rearrangements of Individual Nucleotides during RNA-Ligand Binding Are Rate-Differentiated. *Journal of the American Chemical Society* **138**, 3627-3630, doi:10.1021/jacs.5b11876 (2016).

27 Lu, X., Kong, K. Y. S. & Unrau, P. J. Harmonizing the growing fluorogenic RNA aptamer toolbox for RNA detection and imaging. *Chemical Society reviews* **52**, 4071-4098, doi:10.1039/d3cs00030c (2023).

28 Huang, K. *et al.* Structure-based investigation of fluorogenic Pepper aptamer. *Nature chemical biology* **17**, 1289-1295, doi:10.1038/s41589-021-00884-6 (2021).

29 Huang, K. *et al.* Structural basis of a small monomeric Clivia fluorogenic RNA with a large Stokes shift. *Nature chemical biology* **20**, 1453-1460, doi:10.1038/s41589-024-01633-1 (2024).

30 Zhang, Y. *et al.* Structural mechanisms for binding and activation of a contact-quenched fluorophore by RhoBAST. *Nature Communications* **15**, 4206, doi:10.1038/s41467-024-48478-9 (2024).

31 Siwik, Shea H. *et al.* Structural basis for ring-opening fluorescence by the RhoBAST RNA aptamer. *Nucleic acids research* **53**, doi:10.1093/nar/gkaf555 (2025).

32 Li, H. *et al.* Ligand specificity and adaptability revealed by the first Guanine-II riboswitch tertiary structure. *Nucleic acids research* **53**, doi:10.1093/nar/gkaf884 (2025).

33 Shen, X. *et al.* Structure-based insights into the ligand specificity tuning of 2′-dG-III riboswitch. *Nucleic acids research* **53**, doi:10.1093/nar/gkaf773 (2025).

34 Zheng, L. *et al.* Structure-based insights into recognition and regulation of SAM-sensing riboswitches. *Science China Life Sciences* **66**, 31-50, doi:10.1007/s11427-022-2188-7 (2023).

35 Li, C. *et al.* Structure-based characterization and compound identification of the wild-type THF class-II riboswitch. *Nucleic acids research* **52**, 8454-8465, doi:10.1093/nar/gkae377 (2024).

36 Stoddard, C. D. *et al.* Free state conformational sampling of the SAM-I riboswitch aptamer domain. *Structure* **18**, 787-797, doi:10.1016/j.str.2010.04.006 (2010).

37 Wong, F. *et al.* Deep generative design of RNA aptamers using structural predictions. *Nat Comput Sci* **4**, 829-839, doi:10.1038/s43588-024-00720-6 (2024).

38 Arora, A., Sunbul, M. & Jäschke, A. Dual-colour imaging of RNAs using quencher- and fluorophore-binding aptamers. *Nucleic Acids Research* **43**, e144-e144, doi:10.1093/nar/gkv718 (2015).

39 Vonrhein, C. *et al.* Data processing and analysis with the autoPROC toolbox. *Acta Crystallogr D Biol Crystallogr* **67**, 293-302, doi:10.1107/s0907444911007773 (2011).

40 Adams, P. D. *et al.* PHENIX: a comprehensive Python-based system for macromolecular structure solution. *Acta Crystallogr D Biol Crystallogr* **66**, 213-221, doi:10.1107/s0907444909052925 (2010).

41 Emsley, P. & Cowtan, K. Coot: model-building tools for molecular graphics. *Acta crystallographica. Section D, Biological crystallography* **60**, 2126-2132, doi:10.1107/s0907444904019158 (2004).

42 Murshudov, G. N., Vagin, A. A. & Dodson, E. J. Refinement of macromolecular structures by the maximum-likelihood method. *Acta crystallographica. Section D, Biological crystallography* **53**, 240-255, doi:10.1107/s0907444996012255 (1997).

43 Chen, H. *et al.* Structural distinctions between NAD+ riboswitch domains 1 and 2 determine differential folding and ligand binding. *Nucleic acids research* **48**, 12394-12406, doi:10.1093/nar/gkaa1029 (2020).

Extended Data Figure Captions

Extended Data Figure 1 | Original RhoBAST sequence and spectra of TMR-DN and RhoBAST/TMR-DN. a. The initial sequence and second structure of RhoBAST selected through SELEX[1]. **b.** Normalized excitation and emission spectra of free TMR-DN and RhoBAST/TMR-DN complex in buffer containing 20 mM HEPES at pH 7.4, 125 mM KCl, 5 mM $MgCl_2$, and 0.05% Tween 20.

Extended Data Figure 2 | Alignment of the free-form and TMR-DN-bound-form RhoBAST structures. a. Overall structural alignment of RhoBAST in the free-form (in green) and TMR-DN-bound-form (in blue). **b-c.** Two elongated helices served as scaffolds of the free-form **(b)** and TMR-DN-bound-form **(c)** RhoBAST. The coaxial stacking of P1 and P3 forms an elongated helix, which serves as the primary structural scaffold of RhoBAST. The J2/3 terminus base pair and the J2/3-L3 inter-base pair coaxially stack with P2, forming the lateral scaffold of RhoBAST.

Extended Data Figure 3 | Long-range interactions of TMR-DN-bound form RhoBAST. a. The tertiary structure alignment of J2/3 and L3 loop of the free-form (in green) and TMR-DN-bound-form (in bule) RhoBAST. **b.** Cartoon representation of the tertiary structure of TMR-DN-bound form RhoBAST, with nucleotides involved in long-range interactions highlighted in stick rendering. **c.** Structural organization of junction J2/3 and close-up view of the interactions between junction J2/3 and terminal loop L3. **d-g.** Close-up view of the base triple A24(J2/3)-A37(L3)-A42(L3) (**d**), G26 (J2/3)-A43 (L3)-A36 (L3) (**e**), G23(J2/3)-C44(L3) (**f**), G27(J2/3)-C35(L3) (**g**).

Extended Data Figure 4 | Computational mutagenesis of residue 38 reveals energetically preferred purine bases. a. The tertiary structure alignment of the top terminal region of RhoBAST residue 38 mutants in their ligand-binding states. G38 is shown in green, A38 is shown in pink, C38 is shown in blue, U38 is shown in yellow. **b.** BRIQ folding energy calculations of RhoBAST residue 38 mutants in their ligand-free states. The G38 and A38 variants respectively have average folding energies -

352.813 kcal/mol and -351.765 kcal/mol, while those of the C38 and U38 variants are -348.621 kcal/mol and -348.274 kcal/mol, respectively.

Extended Data Figure 5 | Comparation of the WT, G38A, and G38U RhoBAST structures in their ligand-free states. a. Cartoon representation of the free-form tertiary structure of RhoBAST G38U mutant. **b-d.** The top terminal region spanning (G/A/U)38 to U41 in the WT **(b),** G38A mutant **(c)** and G38U mutant **(d)** tertiary structures exhibits relatively high B factors, indicating elevated conformational flexibility in these regions.

Extended Data Figure 6 | Detailed comparison of RhoBAST-WT and G38A mutant bound with TMR-DN. a. Surface representation of the RhoBAST G38A mutant bound to TMR-DN (shown in spheres). **b.** Cartoon and stick representation of the binding pocket of RhoBAST G38A mutant/TMR-DN complex, with TMR-DN shown in surface. **c.** Close-up view of the top base triple A38-G39-U41. The sugar edge of G39 forms two hydrogen bonds with the Watson-Crick edge of U41, while N7 of G39 interacts with a nitroxide of DN moiety. The carboxyl oxygen of TMR moiety forms two hydrogen bonds with Watson-Crick edge of G39 in the top triple. The 2Fobserve-Fcalculate (2Fo –Fc) composite omit map of TMR-DN contoured at level 1.0 σ is shown. **d.** Overall structural alignment of the WT (in green) and G38A (in pink) RhoBAST in their ligand-bound states. **e.** Alignment of L3 region between RhoBAST-WT and RhoBAST G38A mutant in their ligand-bound states. A38 is closely resembled G38 of the wild-type TMR-DN-bound complex, with the exception of U40, which remains relatively flexible.

Extended Data Figure 7 | Alignment of the free-form and TMR-DN-bound-form RhoBAST G38A mutant structures. a. Overall structural alignment of the free-form (in blue) and TMR-DN-bound-form (in gray) RhoBAST G38A mutant. **b.** Structural alignment of L3 region between free-form and TMR-DN-bound form of RhoBAST G38A mutant. A38 exhibits the most pronounced deviation. TMR-DN is shown in stick, Surface representation and cartoon representation of the top terminal region is shown

at the same time.

Extended Data Figure 8 | Comparison among TMR-DN bound complexes of RhoBAST variants. a. Structural alignment of the overall fold among the wild-type (in green) and G38A (in blue) RhoBAST/TMR-DN complexes with the previously reported RhoBAST variant (in grey) (termed Add-UA, PDB: 8JY0). The box highlights the top view and the side view of ligands within the binding pocket, reveals that the TMR moiety are consistently positioned while the DN moiety exhibits positional variability. **b.** Surface representation of the RhoBAST aptamers bound to TMR-DN (ligand are shown in sticks). The binding pocket adopts a distinctive finger-and-palm-like conformation.

Extended Data Figure 9 | The tertiary structure and Surface plasmon resonance (SPR) assay of the RhoBAST aptamer bound with TMR and 5-TAMRA. a. Chemical structures of the fluorophore TMR, TMR-DN and 5-TAMRA, in which the R group is replaced by -H, -DN moiety and -COOH, respectively. **b-c.** SPR analysis of the RhoBAST aptamer binding affinity and kinetics with 5-TAMRA **(b)** and TMR **(c). d-e.** Cartoon representation of the tertiary structure of the RhoBAST aptamer bound to 5-TAMRA **(d)** and TMR **(e)** (shown in spheres)**.**

Extended Data Figure 10 | Structural comparison of RhoBAST bound with TMR-DN, TMR and 5-TAMRA. a. Structural alignment of the RhoBAST aptamer bound to TMR (in pink) and TMR-DN yielding an RMSD of 1.098 Å. **b.** Structural alignment of the RhoBAST aptamer bound to 5-TAMRA (in cyan) and TMR-DN yielding an RMSD of 0.673 Å. **c.** Overall structural alignment of RhoBAST bound with TMR-DN (shown in sphere), TMR (shown in pink stick) and 5-TAMRA (shown in cyan stick). The RNA scaffold colors of TMR and 5-T AMRA correspond to the color of ligand. **d-e.** Surface representation of the RhoBAST aptamer bound to TMR **(d)** and 5-TAMRA **(e)**.

Supplementary Figure Caption

Supplementary Figure 1 | Anomalous difference electron density map for selenourea-soaked TMR-bound RhoBAST crystals. Anomalous electron density map contoured at level 3.0 σ for Se sites (orange balls, labelled with red arrow) in one asymmetric unit of TMR-bound RhoBAST, which were used to solve the phase problem of the structure.

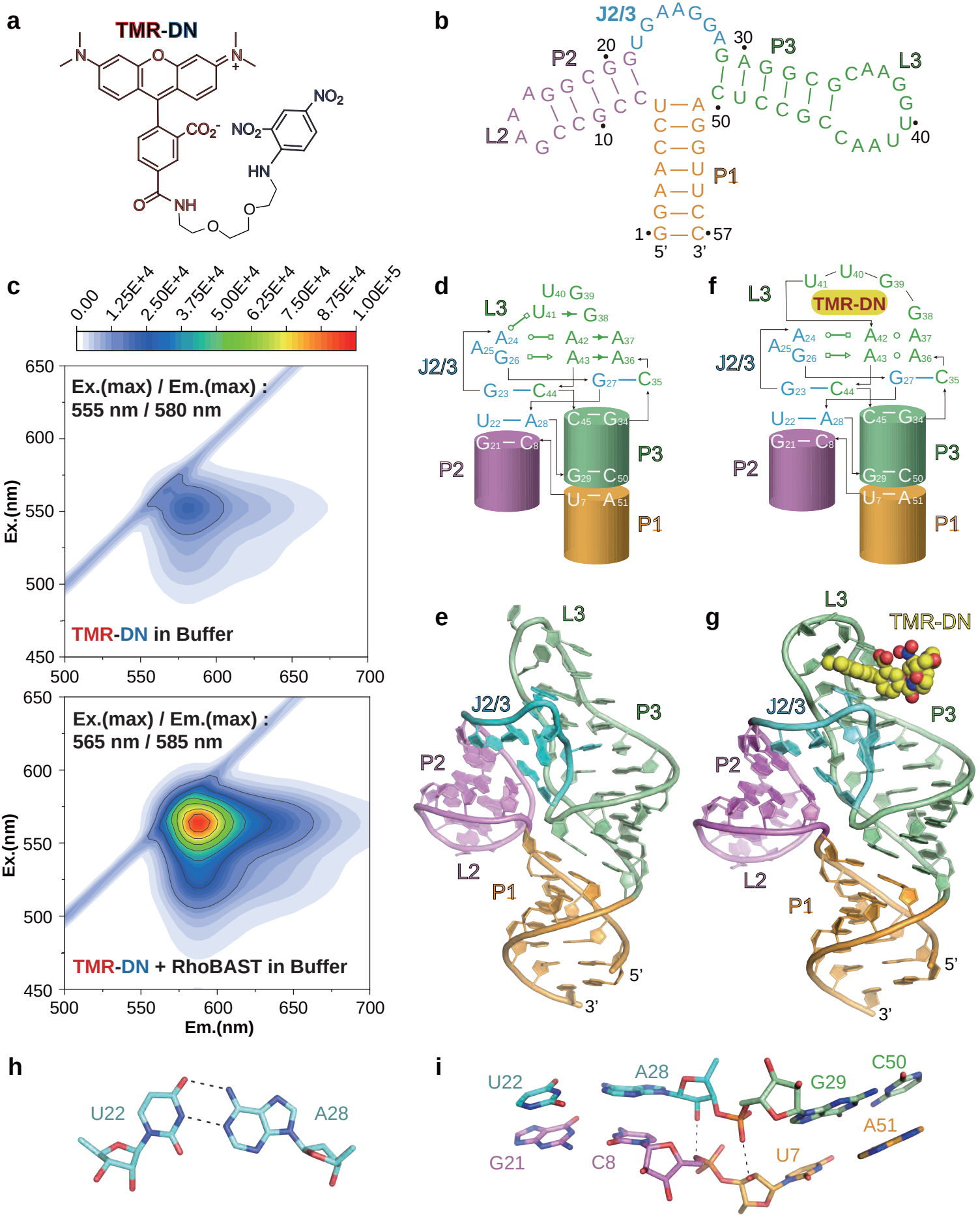
a
TMR-DN
b
J2/3
P2
P3
L3
L2
P1
c
Ex.(max) / Em.(max) :
555 nm / 580 nm
TMR-DN in Buffer
Ex.(max) / Em.(max) :
565 nm / 585 nm
TMR-DN + RhoBAST in Buffer
Ex.(nm)
Em.(nm)
d
f
TMR-DN
e
g
5'
3'
h
U22
A28
i
U22
A28
G29
C50
A51
G21
C8
U7

Figure 1

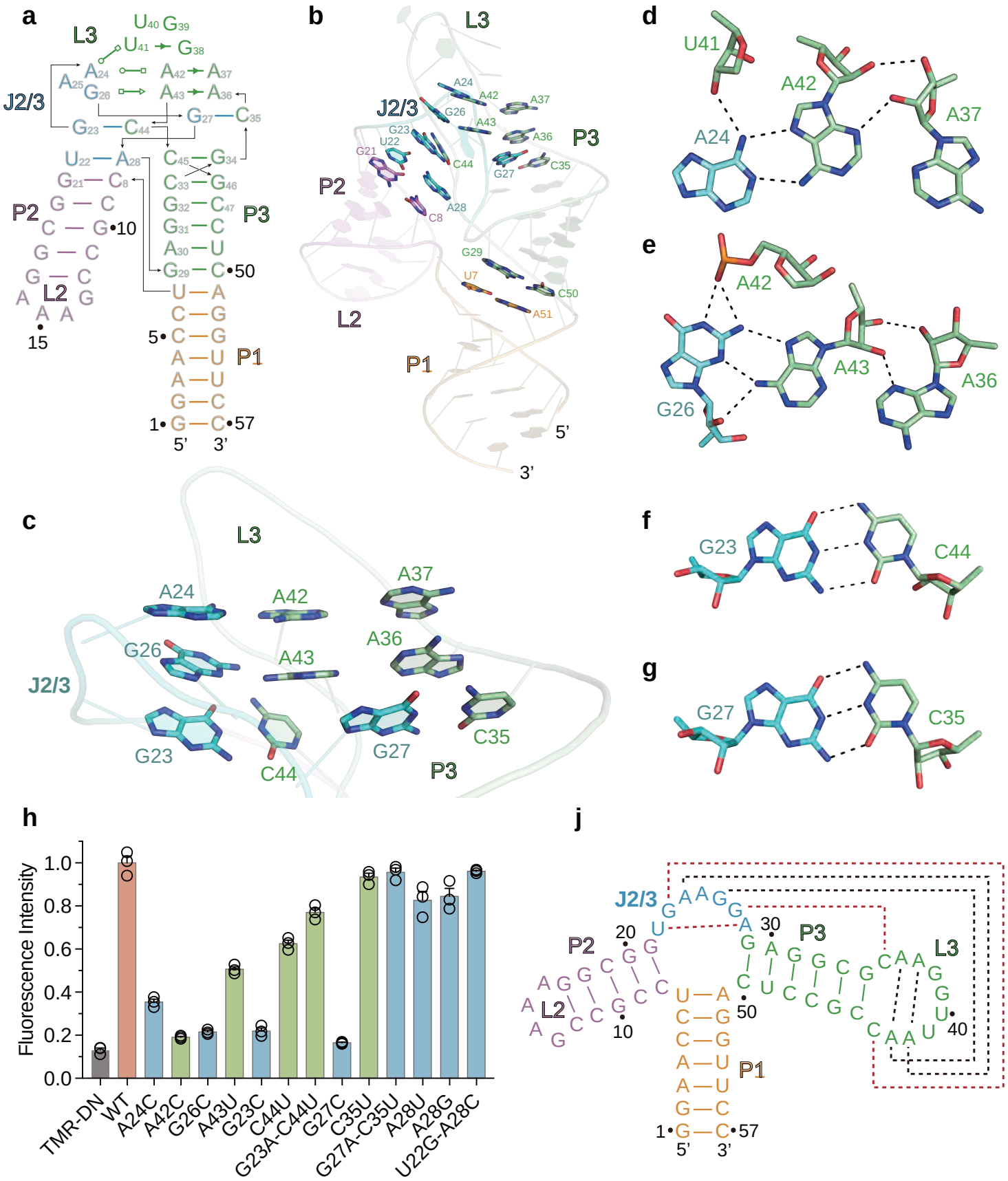
a
L3
J2/3
P2
P3
P1
L2
b
L3
J2/3
P2
P3
L2
P1
5'
3'
c
L3
J2/3
d
e
f
g
h
Fluorescence Intensity
TMR-DN
WT
A24C
A42C
G26C
A43U
G23C
C44U
G23A-C44U
G27C
C35U
G27A-C35U
A28U
A28G
U22G-A28C
j
J2/3
P2
P3
L3
L2
P1

Figure 2

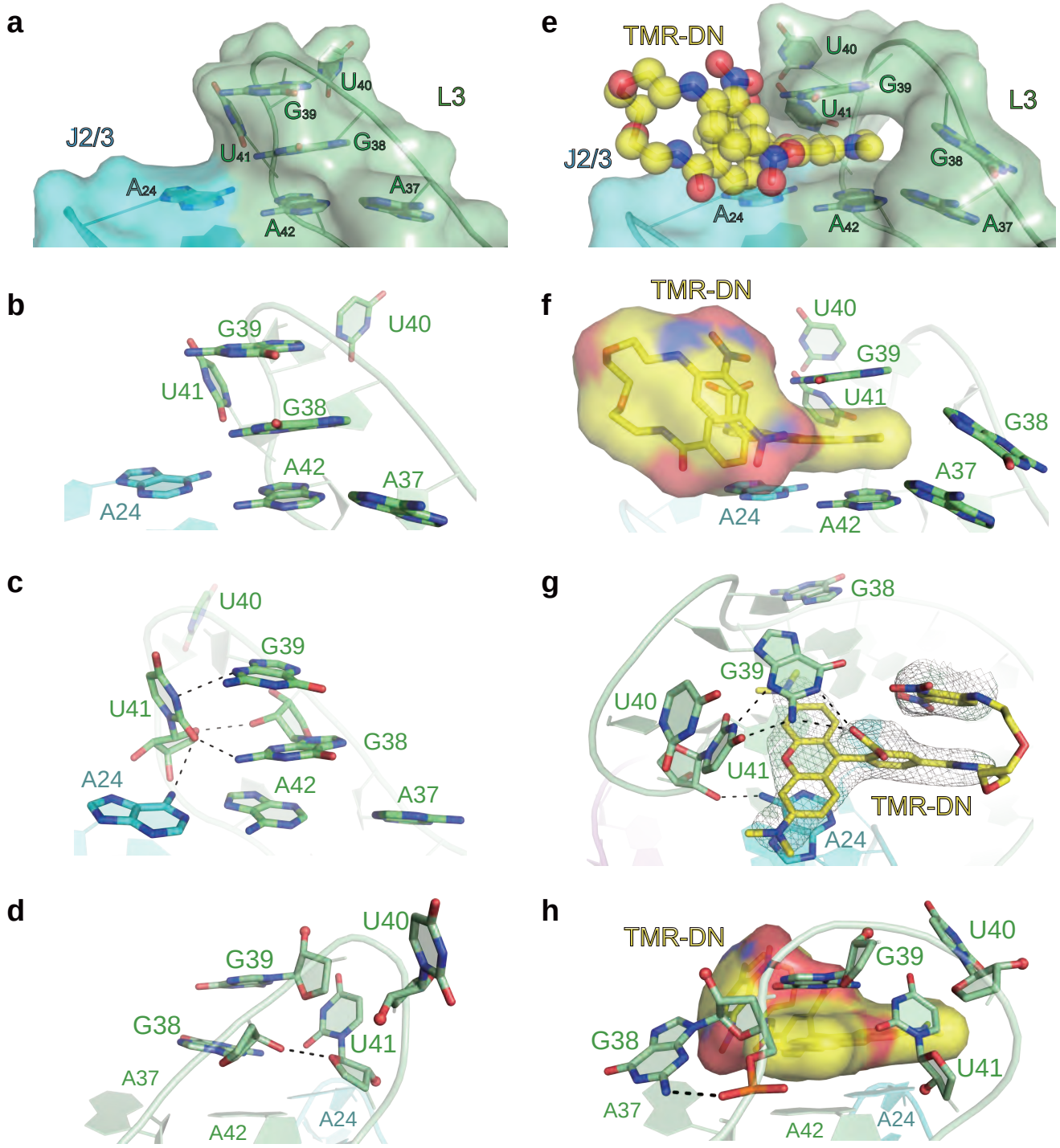
a
J2/3
U40
L3
G39
U41
G38
A24
A37
A42
b
G39
U40
U41
G38
A42
A37
A24
c
U40
G39
U41
G38
A24
A42
A37
d
U40
G39
G38
U41
A37
A42
A24
e
TMR-DN
U40
G39
L3
U41
J2/3
G38
A24
A42
A37
f
TMR-DN
U40
G39
U41
G38
A37
A24
A42
g
G38
G39
U40
U41
TMR-DN
A24
h
TMR-DN
U40
G39
G38
U41
A37
A42
A24

Figure 3

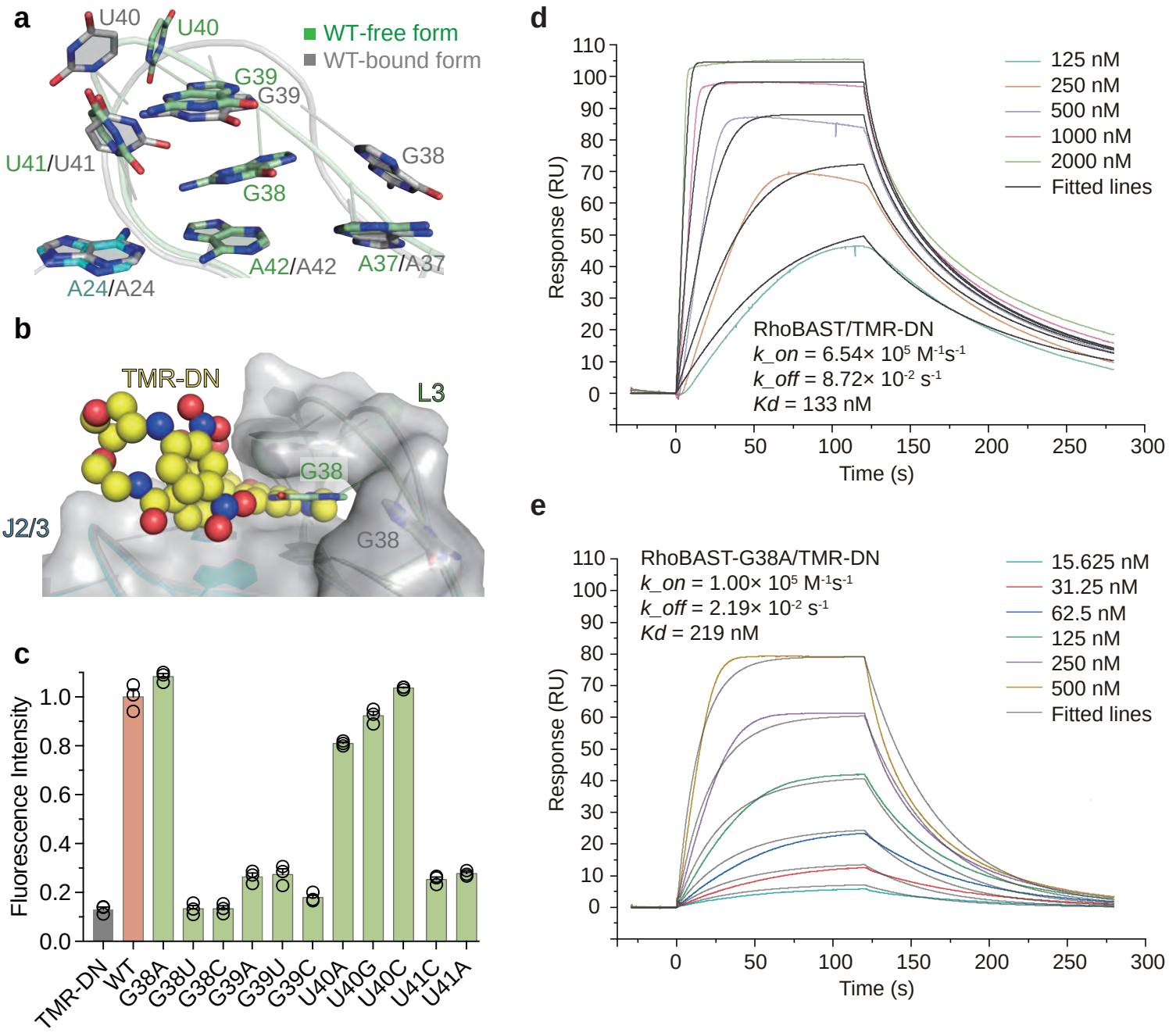
a
U40
U40
WT-free form
WT-bound form
G39
G39
U41/U41
G38
G38
A24/A24
A42/A42
A37/A37
b
TMR-DN
L3
G38
J2/3
G38
c
Fluorescence Intensity
0.0
0.2
0.4
0.6
0.8
1.0
TMR-DN
WT
G38A
G38U
G38C
G39A
G39U
G39C
U40A
U40G
U40C
U41C
U41A
d
Response (RU)
0
10
20
30
40
50
60
70
80
90
100
110
0
50
100
150
200
250
300
Time (s)
125 nM
250 nM
500 nM
1000 nM
2000 nM
Fitted lines
RhoBAST/TMR-DN
k_on = 6.54× 10^5 M^-1s^-1
k_off = 8.72× 10^-2 s^-1
Kd = 133 nM
e
Response (RU)
0
10
20
30
40
50
60
70
80
90
100
110
0
50
100
150
200
250
300
Time (s)
RhoBAST-G38A/TMR-DN
k_on = 1.00× 10^5 M^-1s^-1
k_off = 2.19× 10^-2 s^-1
Kd = 219 nM
15.625 nM
31.25 nM
62.5 nM
125 nM
250 nM
500 nM
Fitted lines

Figure 4

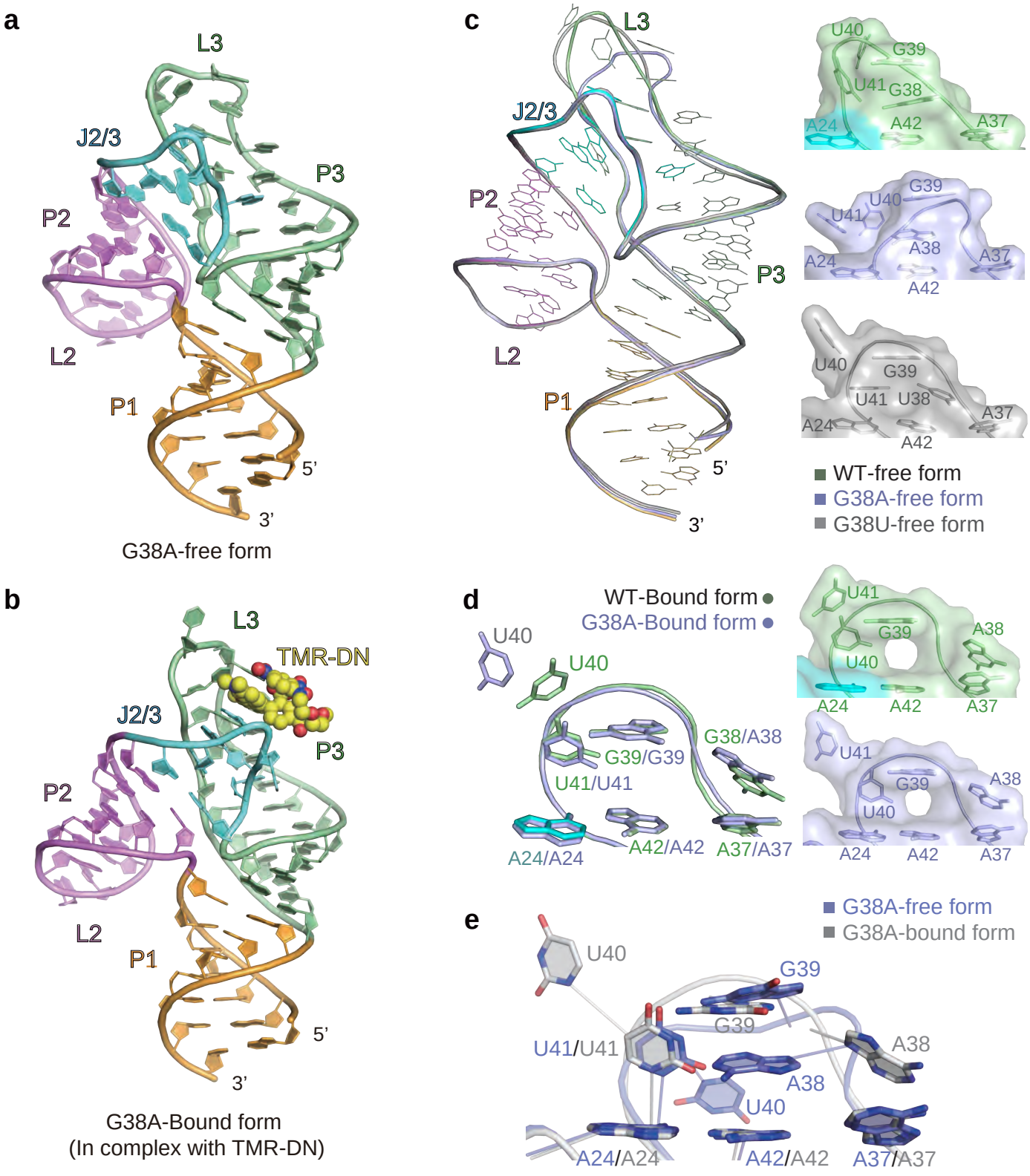
a
L3
J2/3
P3
P2
L2
P1
5'
3'
G38A-free form
b
L3
TMR-DN
J2/3
P3
P2
L2
P1
5'
3'
G38A-Bound form
(In complex with TMR-DN)
c
L3
J2/3
P2
P3
L2
P1
5'
3'
U40
G39
U41
G38
A24
A42
A37
G39
U40
U41
A38
A24
A37
A42
U40
G39
U41
U38
A37
A24
A42
WT-free form
G38A-free form
G38U-free form
d
WT-Bound form
G38A-Bound form
U40
U40
G38/A38
G39/G39
U41/U41
A24/A24
A42/A42
A37/A37
U41
G39
A38
U40
A24
A42
A37
U41
G39
A38
U40
A24
A42
A37
e
G38A-free form
G38A-bound form
U40
G39
G39
U41/U41
A38
A38
U40
A24/A24
A42/A42
A37/A37

Figure 5

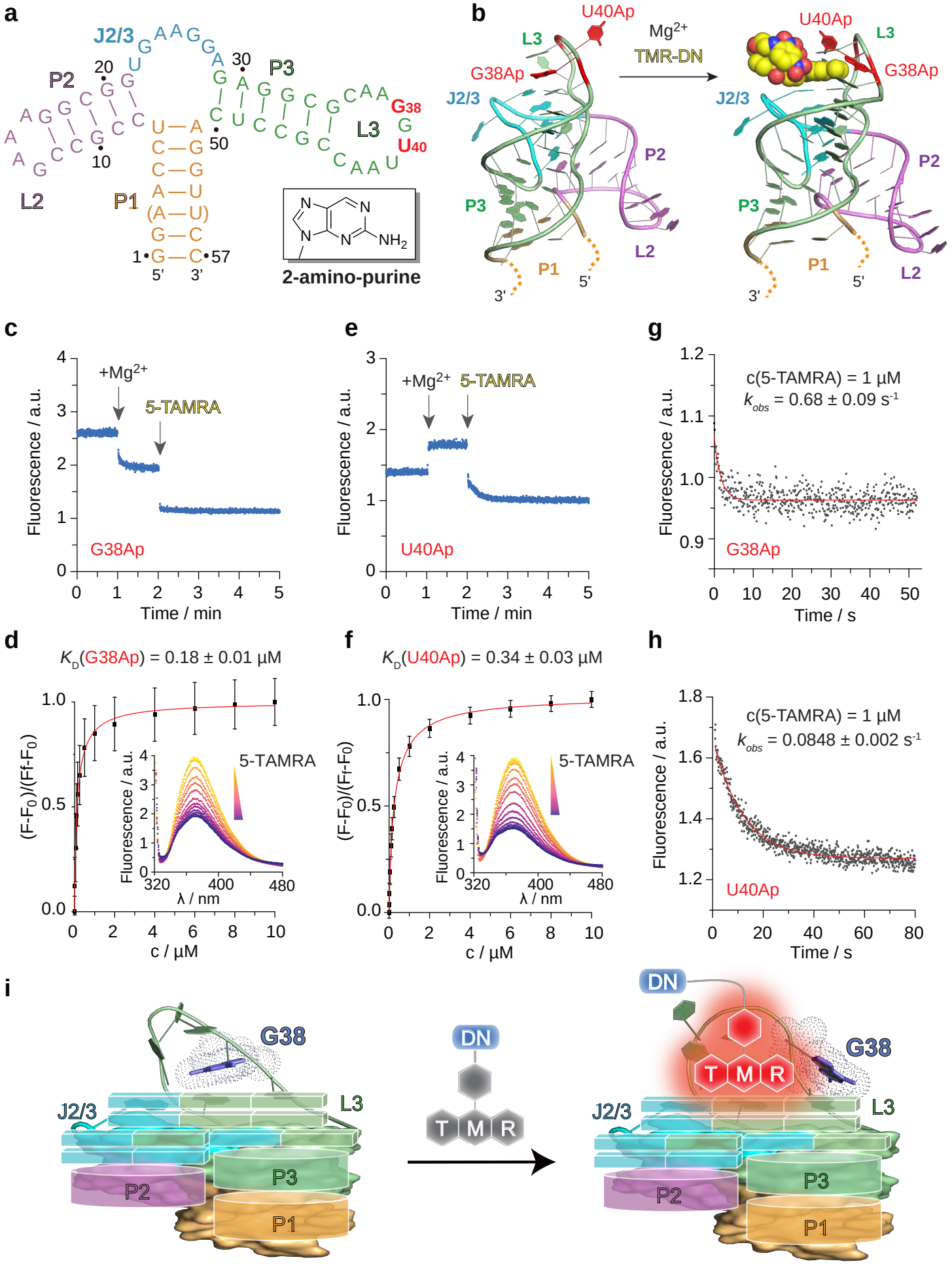
a
J2/3
P2
P3
L3
G38
U40
L2
P1
2-amino-purine
b
U40Ap
L3
G38Ap
J2/3
P2
P3
L2
P1
Mg2+
TMR-DN
c
+Mg2+
5-TAMRA
G38Ap
Fluorescence / a.u.
Time / min
e
+Mg2+
5-TAMRA
U40Ap
Fluorescence / a.u.
Time / min
g
c(5-TAMRA) = 1 µM
kobs = 0.68 ± 0.09 s-1
G38Ap
Fluorescence / a.u.
Time / s
d
KD(G38Ap) = 0.18 ± 0.01 µM
(F-F0)/(Ff-F0)
5-TAMRA
Fluorescence / a.u.
λ / nm
c / µM
f
KD(U40Ap) = 0.34 ± 0.03 µM
(F-F0)/(Ff-F0)
5-TAMRA
Fluorescence / a.u.
λ / nm
c / µM
h
c(5-TAMRA) = 1 µM
kobs = 0.0848 ± 0.002 s-1
U40Ap
Fluorescence / a.u.
Time / s
i
G38
J2/3
L3
P2
P3
P1
DN
T M R
DN
G38
T M R
J2/3
L3
P2
P3
P1

Figure 6

Extended Data Figures

Dynamic nucleotide flipping drives super-resolution fluorescence activation in the RhoBAST RNA aptamer

Xiaoqing Tai[1,6], Mengqi He[1,6], Christoph Mitteregger[2,6], Huiqin You[1], Peng Xiong[3,4], Zejia Hu[1], Xinyue Bao[1], Xin Shen[1], Hongcheng Li[1], Yu Li[5], Jinzhu Zhang[1,*], Ronald Micura[2,*] and Aiming Ren[1,*]

[1]Department of Cardiology of The Second Affiliated Hospital and Life Sciences Institute and School of Medicine and Liangzhu Laboratory, Zhejiang University, Hangzhou 310058, China

[2]Institute of Organic Chemistry, Center for Molecular Biosciences Innsbruck, Leopold Franzens University, Innsbruck A6020, Austria

[3]School of Biomedical Engineering, Division of Life Sciences and Medicine, University of Science and Technology of China, Hefei, Anhui 230026, China

[4]Suzhou Institute for Advanced Research, University of Science and Technology of China, Suzhou, Jiangsu 215123, China

[5]Department of Computer Science and Engineering, The Chinese University of Hong Kong, Hong Kong SAR 000000, China

[6]These authors contributed equally to this work.

*Email: aimingren@zju.edu.cn (AR), ronald.micura@uibk.ac.at (RM) and jinzhuzhang@zju.edu.cn (JZ).

Contents

Extended Data Figures

Extended Data Figures

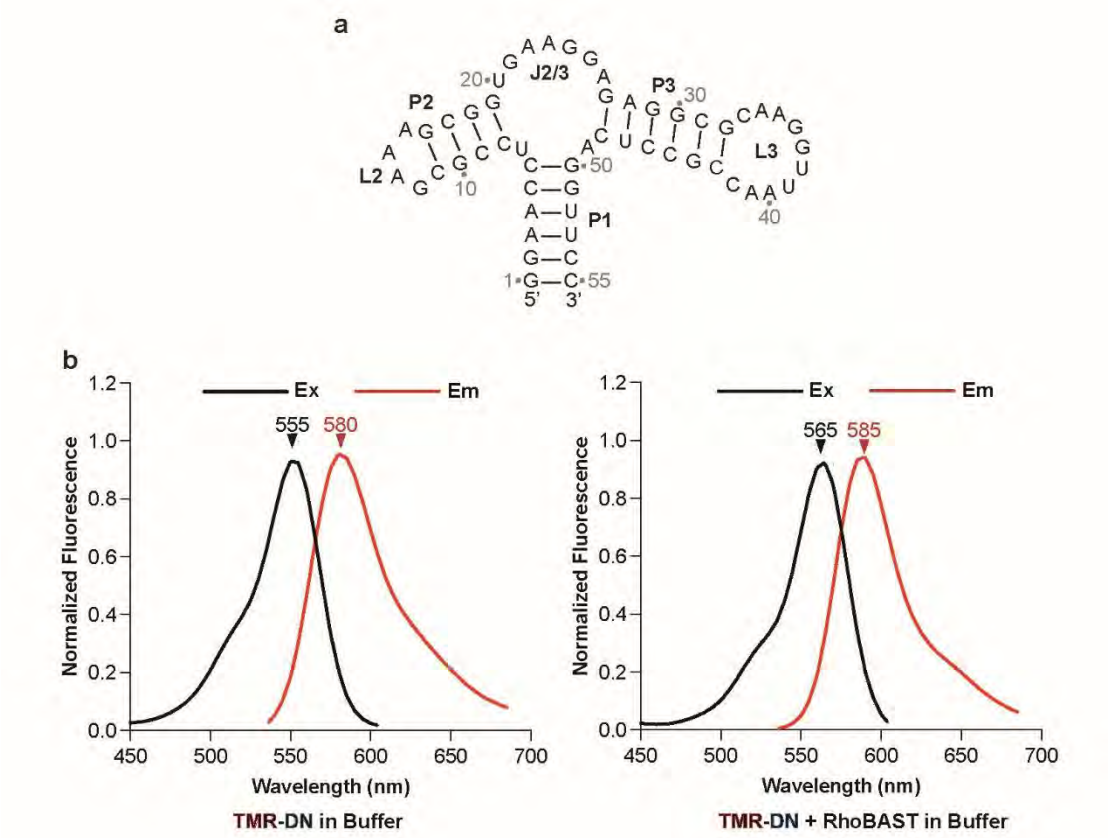

Extended Data Figure 1 | Original RhoBAST sequence and spectra of TMR-DN and RhoBAST/TMR-DN. a. The initial sequence and second structure of RhoBAST selected through SELEX[1]. **b.** Normalized excitation and emission spectra of free TMR-DN and RhoBAST/TMR-DN complex in buffer containing 20 mM HEPES at pH 7.4, 125 mM KCl, 5 mM $MgCl_2$, and 0.05% Tween 20.

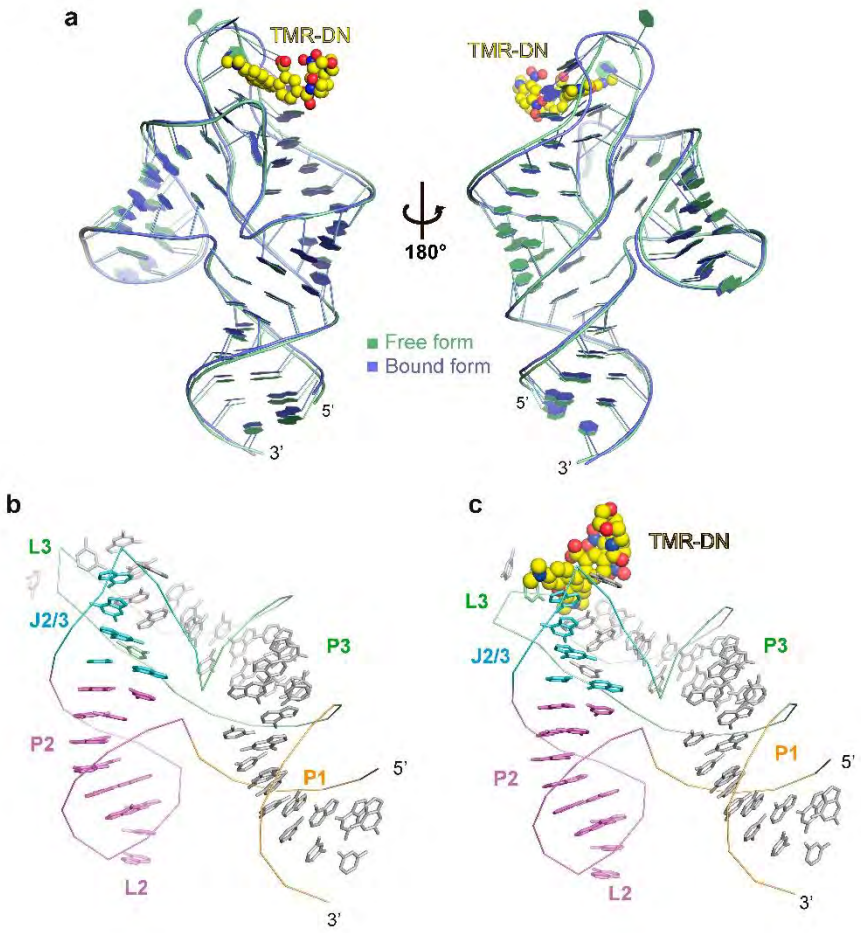

Extended Data Figure 2 | Alignment of the free-form and TMR-DN-bound-form RhoBAST structures. a. Overall structural alignment of RhoBAST in the free-form (in green) and TMR-DN-bound-form (in blue). **b-c.** Two elongated helices served as scaffolds of the free-form **(b)** and TMR-DN-bound-form **(c)** RhoBAST. The coaxial stacking of P1 and P3 forms an elongated helix, which serves as the primary structural scaffold of RhoBAST. The J2/3 terminus base pair and the J2/3-L3 inter-base pair coaxially stack with P2, forming the lateral scaffold of RhoBAST.

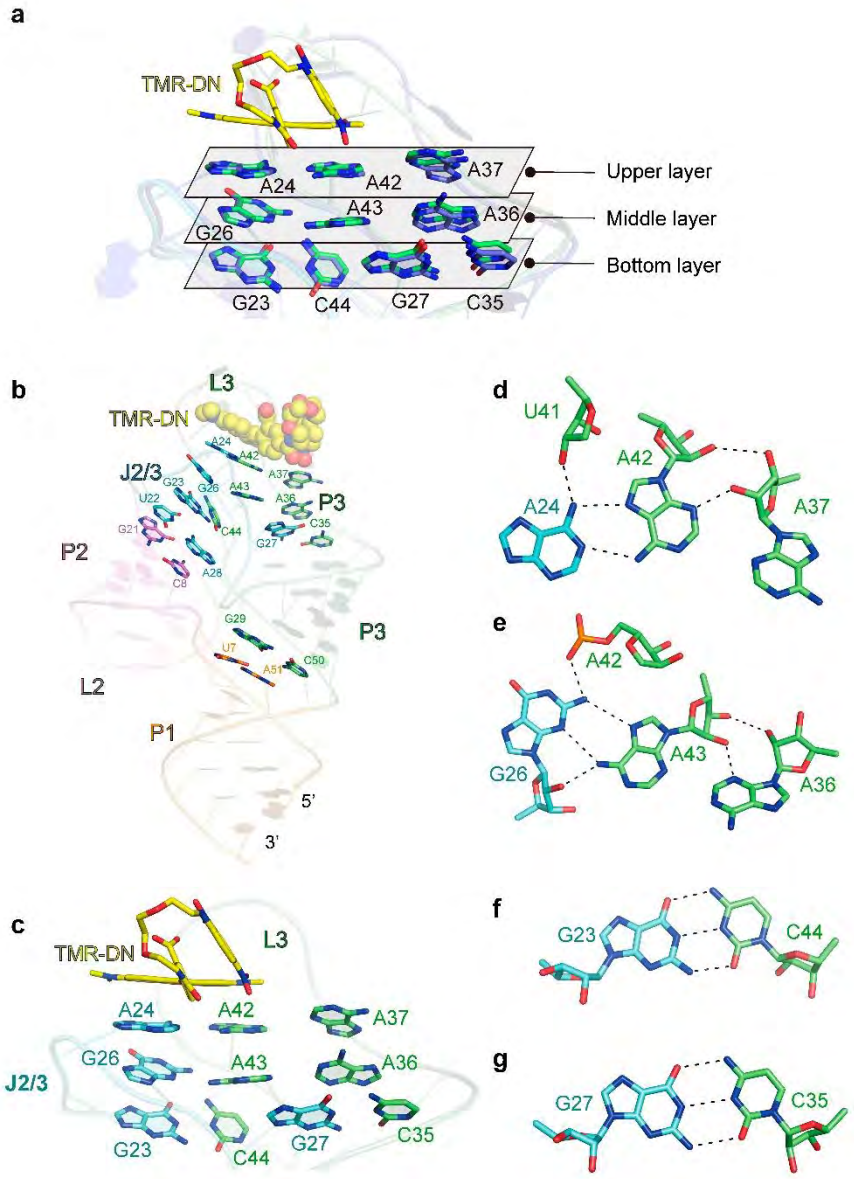

Extended Data Figure 3 | Long-range interactions of TMR-DN-bound form RhoBAST. a. The tertiary structure alignment of J2/3 and L3 loop of the free-form (in green) and TMR-DN-bound-form (in bule) RhoBAST. **b.** Cartoon representation of the tertiary structure of TMR-DN-bound form RhoBAST, with nucleotides involved in long-range interactions highlighted in stick rendering. **c.** Structural organization of junction J2/3 and close-up view of the interactions between junction J2/3 and terminal loop L3. **d-g.** Close-up view of the base triple A24(J2/3)-A37(L3)-A42(L3) (**d**), G26 (J2/3)-A43 (L3)-A36 (L3) (**e**), G23(J2/3)-C44(L3) (**f**), G27(J2/3)-C35(L3) (**g**).

a

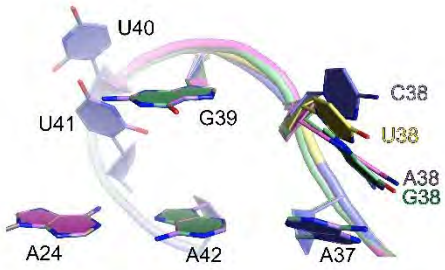

b

Mutant	$G38_{cal}$	$A38_{cal}$	$C38_{cal}$	$U38_{cal}$
Optimized Conformation	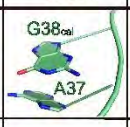		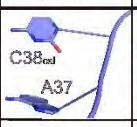	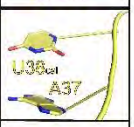
Energy (kcal/mol)	-352.813	-351.765	-348.621	-348.274

Extended Data Figure 4 | Computational mutagenesis of residue 38 reveals energetically preferred purine bases. a. The tertiary structure alignment of the top terminal region of RhoBAST residue 38 mutants in their ligand-binding states. G38 is shown in green, A38 is shown in pink, C38 is shown in blue, U38 is shown in yellow. **b.** BRIQ folding energy calculations of RhoBAST residue 38 mutants in their ligand-free states. The G38 and A38 variants respectively have average folding energies -352.813 kcal/mol and -351.765 kcal/mol, while those of the C38 and U38 variants are -348.621 kcal/mol and -348.274 kcal/mol, respectively.

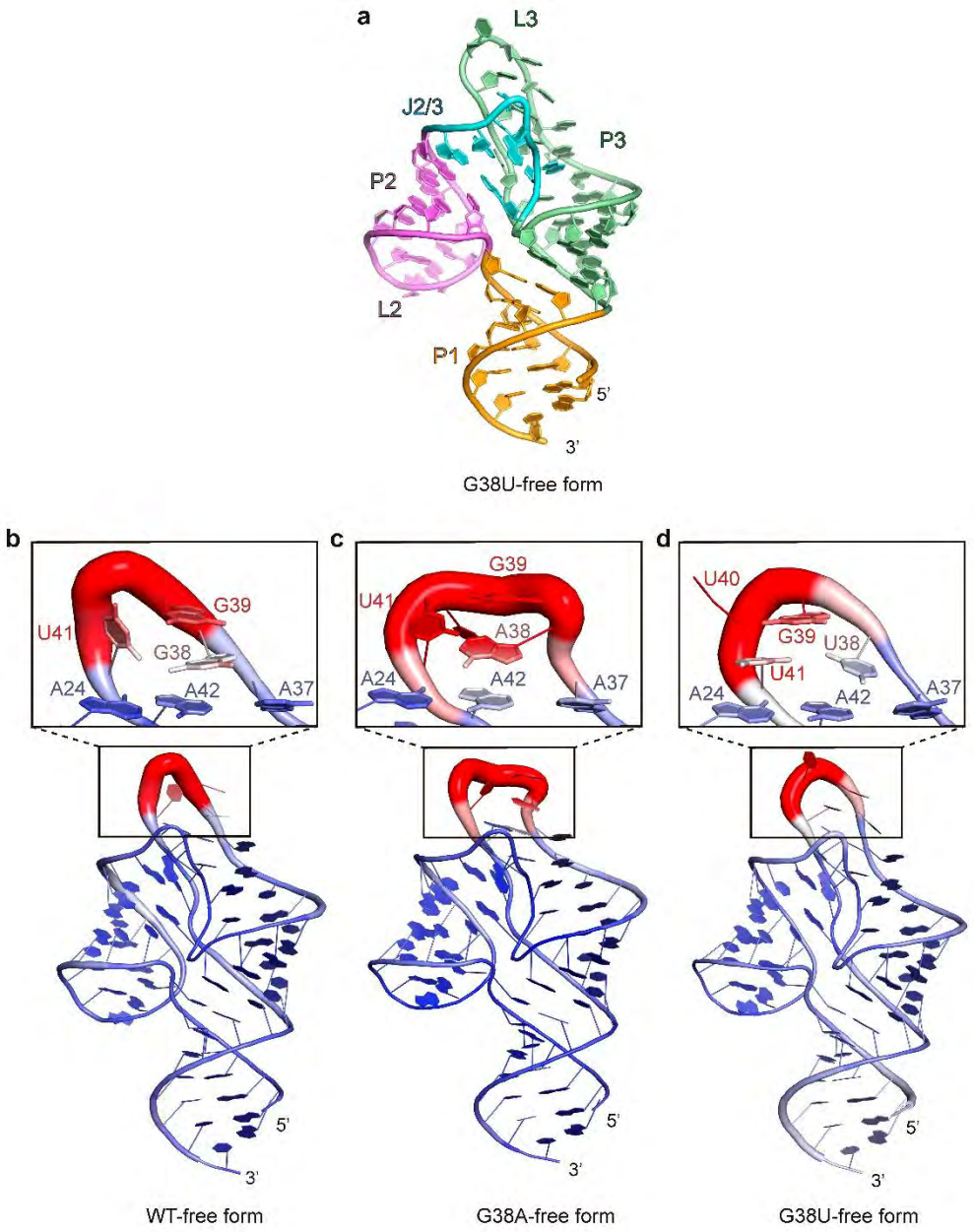

Extended Data Figure 5 | Comparation of the WT, G38A, and G38U RhoBAST structures in their ligand-free states. a. Cartoon representation of the free-form tertiary structure of RhoBAST G38U mutant. **b-d.** The top terminal region spanning (G/A/U)38 to U41 in the WT **(b),** G38A mutant **(c)** and G38U mutant **(d)** tertiary structures exhibits relatively high B factors, indicating elevated conformational flexibility in these regions.

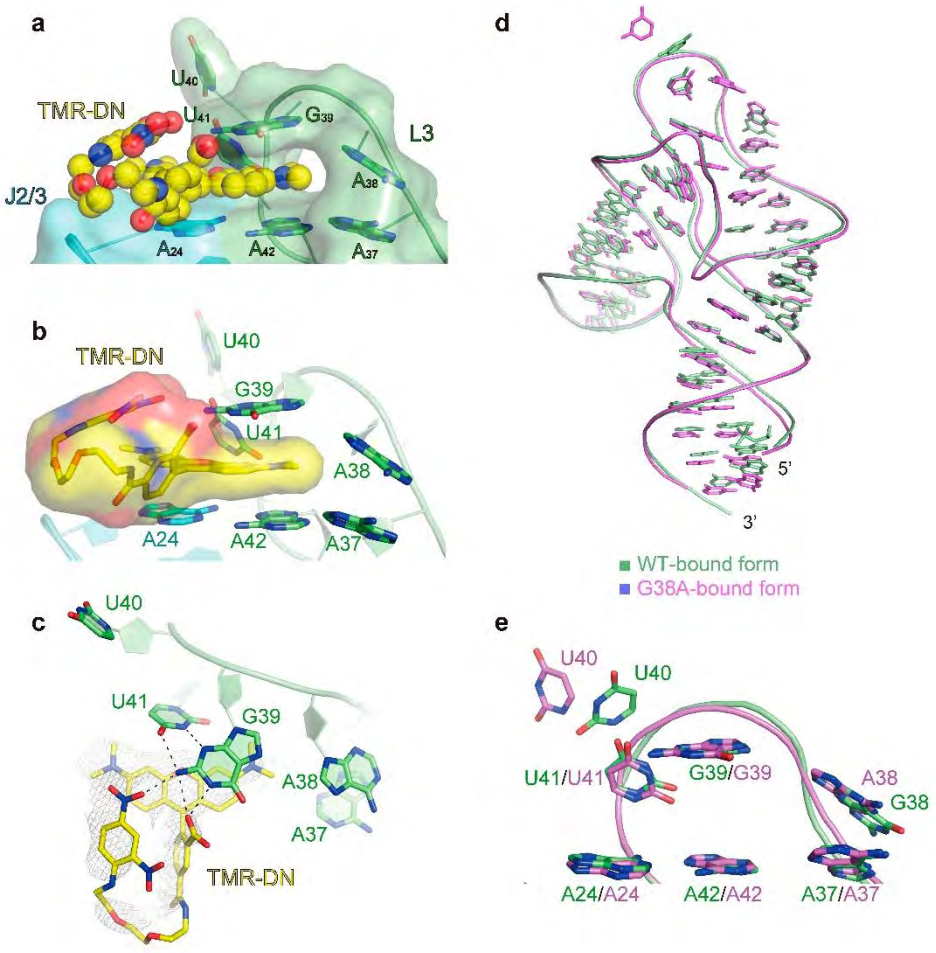

Extended Data Figure 6 | Detailed comparison of RhoBAST-WT and G38A mutant bound with TMR-DN. a. Surface representation of the RhoBAST G38A mutant bound to TMR-DN (shown in spheres). **b.** Cartoon and stick representation of the binding pocket of RhoBAST G38A mutant/TMR-DN complex, with TMR-DN shown in surface. **c.** Close-up view of the top base triple A38-G39-U41. The sugar edge of G39 forms two hydrogen bonds with the Watson-Crick edge of U41, while N7 of G39 interacts with a nitroxide of DN moiety. The carboxyl oxygen of TMR moiety forms two hydrogen bonds with Watson-Crick edge of G39 in the top triple. The 2Fobserve-Fcalculate (2Fo –Fc) composite omit map of TMR-DN contoured at level 1.0 σ is shown. **d.** Overall structural alignment of the WT (in green) and G38A (in pink) RhoBAST in their ligand-bound states. **e.** Alignment of L3 region between RhoBAST-WT and RhoBAST G38A mutant in their ligand-bound states. A38 is closely resembled G38 of the wild-type TMR-DN-bound complex, with the exception of U40, which remains relatively flexible.

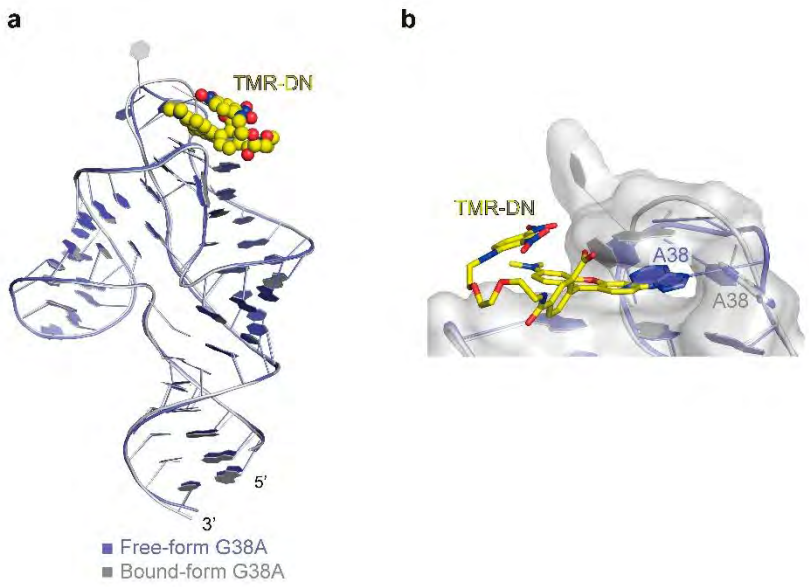

Extended Data Figure 7 | Alignment of the free-form and TMR-DN-bound-form RhoBAST G38A mutant structures. a. Overall structural alignment of the free-form (in blue) and TMR-DN-bound-form (in gray) RhoBAST G38A mutant. **b.** Structural alignment of L3 region between free-form and TMR-DN-bound form of RhoBAST G38A mutant. A38 exhibits the most pronounced deviation. TMR-DN is shown in stick, Surface representation and cartoon representation of the top terminal region is shown at the same time.

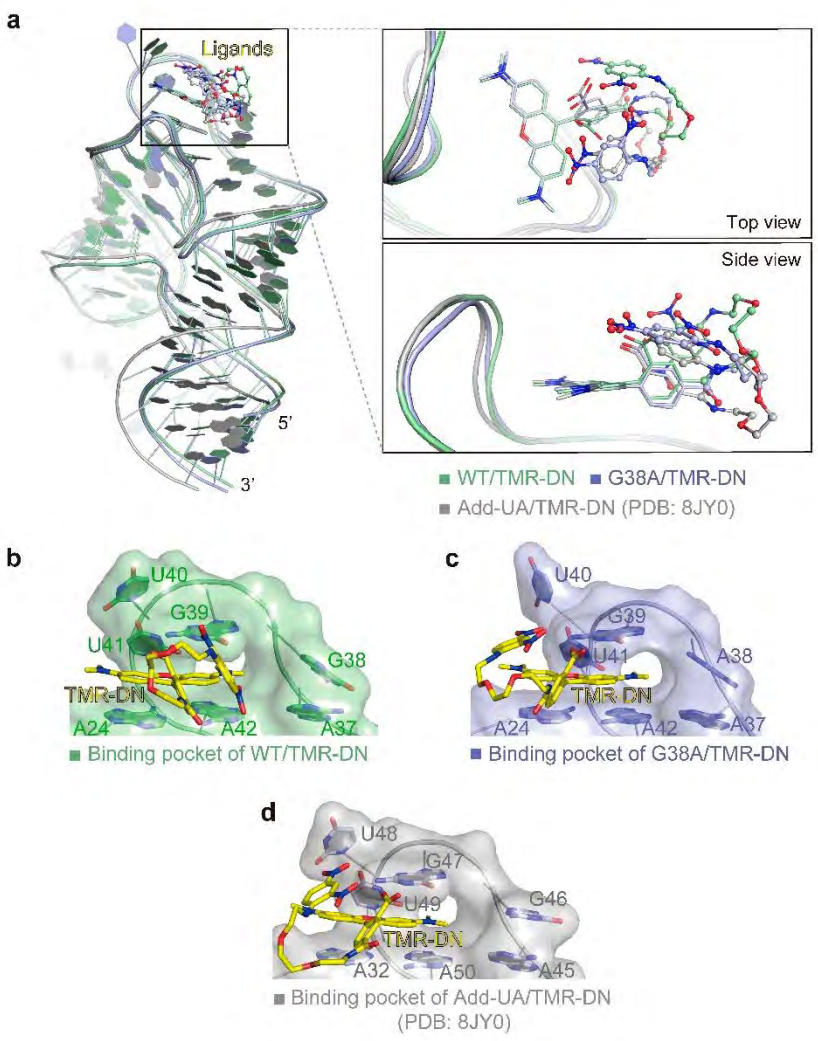

Extended Data Figure 8 | Comparison among TMR-DN bound complexes of RhoBAST variants. a. Structural alignment of the overall fold among the wild-type (in green) and G38A (in blue) RhoBAST/TMR-DN complexes with the previously reported RhoBAST variant (in grey) (termed Add-UA, PDB: 8JY0). The box highlights the top view and the side view of ligands within the binding pocket, reveals that the TMR moiety are consistently positioned while the DN moiety exhibits positional variability. **b.** Surface representation of the RhoBAST aptamers bound to TMR-DN (ligand are shown in sticks). The binding pocket adopts a distinctive finger-and-palm-like conformation.

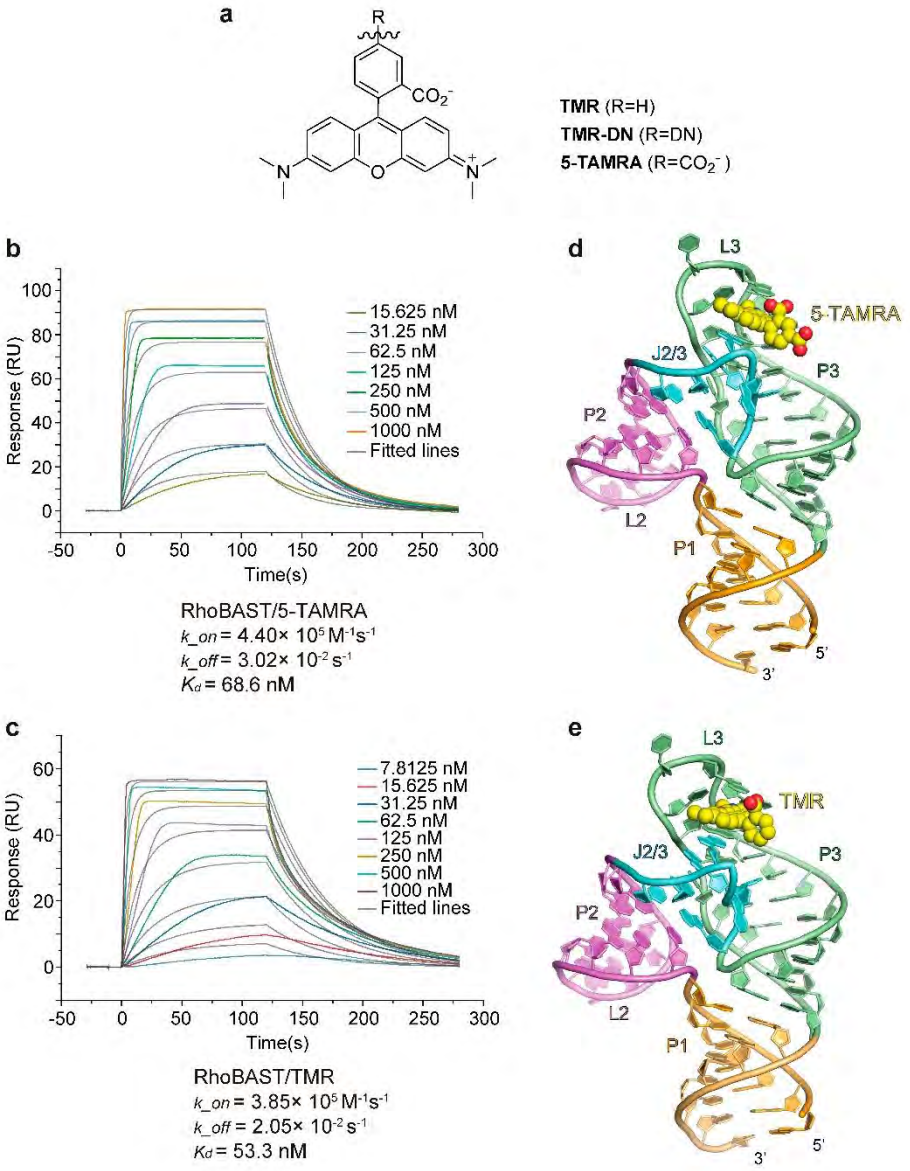

Extended Data Figure 9 | The tertiary structure and Surface plasmon resonance (SPR) assay of the RhoBAST aptamer bound with TMR and 5-TAMRA. a. Chemical structures of the fluorophore TMR, TMR-DN and 5-TAMRA, in which the R group is replaced by -H, -DN moiety and -COOH, respectively. **b-c.** SPR analysis of the RhoBAST aptamer binding affinity and kinetics with 5-TAMRA **(b)** and TMR **(c). d-e.** Cartoon representation of the tertiary structure of the RhoBAST aptamer bound to 5-TAMRA **(d)** and TMR **(e)** (shown in spheres)**.**

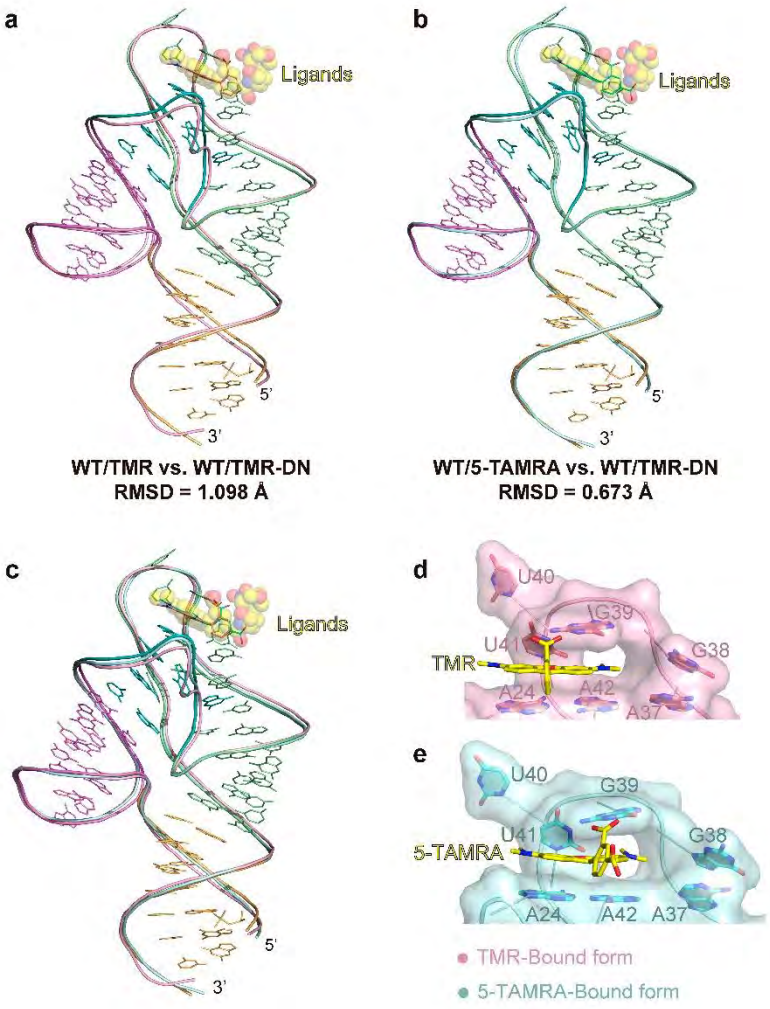

Extended Data Figure 10 | Structural comparison of RhoBAST bound with TMR-DN, TMR and 5-TAMRA. a. Structural alignment of the RhoBAST aptamer bound to TMR (in pink) and TMR-DN yielding an RMSD of 1.098 Å. **b.** Structural alignment of the RhoBAST aptamer bound to 5-TAMRA (in cyan) and TMR-DN yielding an RMSD of 0.673 Å. **c.** Overall structural alignment of RhoBAST bound with TMR-DN (shown in sphere), TMR (shown in pink stick) and 5-TAMRA (shown in cyan stick). The RNA scaffold colors of TMR and 5-T AMRA correspond to the color of ligand. **d-e.** Surface representation of the RhoBAST aptamer bound to TMR **(d)** and 5-TAMRA **(e)**.

References:

1 Sunbul, M. *et al.* Super-resolution RNA imaging using a rhodamine-binding aptamer with fast exchange kinetics. *Nature biotechnology* **39**, 686-690, doi:10.1038/s41587-020-00794-3 (2021).